

## MUSCLE POWER OUTPUT LIMITS FAST-START PERFORMANCE IN FISH

JAMES M. WAKELING\* AND IAN A. JOHNSTON

*Gatty Marine Laboratory, School of Environmental and Evolutionary Biology, University of St Andrews, St Andrews, Fife KY16 8LB, Scotland*

\*e-mail: jmw5@st-andrews.ac.uk

*Accepted 26 February; published on WWW 27 April 1998*

### Summary

Fast-starts associated with escape responses were filmed at the median habitat temperatures of six teleost fish: *Notothenia coriiceps* and *Notothenia rossii* (Antarctica), *Myoxocephalus scorpius* (North Sea), *Scorpaena notata* and *Serranus cabrilla* (Mediterranean) and *Paracirrhites forsteri* (Indo-West-Pacific Ocean). Methods are presented for estimating the spine positions for silhouettes of swimming fish. These methods were used to validate techniques for calculating kinematics and muscle dynamics during fast-starts. The starts from all species show common patterns, with waves of body curvature travelling from head to tail and increasing in amplitude. Cross-validation with sonomicrometry studies allowed gearing ratios between the red and white muscle to be calculated. Gearing ratios must decrease towards the tail with a corresponding change in muscle geometry, resulting in similar white

muscle fibre strains in all the myotomes during the start. A work-loop technique was used to measure mean muscle power output at similar strain and shortening durations to those found *in vivo*. The fast *Sc. notata* myotomal fibres produced a mean muscle-mass-specific power of  $142.7 \text{ W kg}^{-1}$  at  $20^\circ\text{C}$ . Velocity, acceleration and hydrodynamic power output increased both with the travelling rate of the wave of body curvature and with the habitat temperature. At all temperatures, the predicted mean muscle-mass-specific power outputs, as calculated from swimming sequences, were similar to the muscle power outputs measured from work-loop experiments.

Key words: fast-start, skeletal muscle, muscle power output, fish, swimming.

### Introduction

Fast-starts are bursts of high-energy swimming starting either from rest or during periods of steady swimming (Domenici and Blake, 1997). They are used in interactions between predator and prey and are presumably important determinants of survival and feeding success. Fast-starts are largely powered by the recruitment of the fast myotomal muscle since the required strain rate exceeds that of the slower-contracting red muscle fibres (Rome *et al.* 1988; Altringham and Johnston, 1990). Red and white muscle fibres are anatomically distinct in fish myotomes (Alexander, 1969) and so fast-starts provide a good system on which to model muscle action for biologically important behaviours.

Muscle power output is the product of force and its shortening velocity. Estimates of power output were originally derived from steady-state force–velocity relationships measured during isotonic shortening experiments (e.g. Weis-Fogh and Alexander, 1977). The mean muscle-mass-specific power output during a complete contraction cycle was estimated in this way to be  $80 \text{ W kg}^{-1}$  for insect synchronous flight muscle (Ellington, 1985). During the dynamic situation of muscle contraction found in most biological behaviours, however, quasi-steady predictions do not account for the whole muscle performance. The timing of muscle activity relative to

its movement plays a crucial role in determining muscle performance. Maximum power production during a cyclical movement requires the muscle to be fully active during shortening but fully relaxed during lengthening. However, neither activation nor deactivation occurs instantaneously. Muscle force is also modulated by shortening deactivation (Edman, 1980; Ekelund and Edman, 1982) and active prestretch (Edman *et al.* 1978a,b, 1982).

Muscle performance has been modelled for fish using data on activation times and ultrastructure coupled to steady force–velocity characteristics (van Leeuwen *et al.* 1990; van Leeuwen, 1992). These methods have been used to predict muscle function at different longitudinal positions, but not the absolute power output.

The effect of muscle movement can be incorporated into muscle force measurements by using work-loop techniques where isolated fibres are subjected to cyclical length changes whilst the force production is measured. This approach was developed by Machin and Pringle (1959) for asynchronous insect muscle, applied to synchronous insect muscle by Josephson (1985) and first used on fish by Altringham and Johnston (1990). Mean muscle-mass-specific power outputs during complete work loops have been measured at  $130 \text{ W kg}^{-1}$

at 40 °C for the hawkmoth *Manduca sexta* (Stevenson and Josephson, 1990) and 135 W kg<sup>-1</sup> at 35 °C for the lizard *Dipsosaurus dorsalis* (Swoap *et al.* 1993). Work-loop experiments on fish have been refined further by taking direct measurements of the *in vivo* muscle length changes and activation patterns using sonomicrometry and electromyography techniques and then imposing these shortening regimes on isolated fibres *in vitro* (Franklin and Johnston, 1997). These techniques have resulted in fish mean muscle-mass-specific power outputs being measured between 18.1 W kg<sup>-1</sup> at 0 °C for *Notothenia coriiceps* (Franklin and Johnston, 1997) and 75.7 W kg<sup>-1</sup> at 15 °C for *Myoxocephalus scorpius* (G. Temple, personal communication).

Muscle power output can be estimated from the whole-body performance of an animal. During most locomotory activities, the power required for motion must be generated by the muscles. Estimates of the hydrodynamic power requirements for swimming can thus be used to predict a minimum value for fish muscle power output. Frith and Blake (1995) estimated a muscle-mass-specific power output of 300 W kg<sup>-1</sup> at 10 °C for fast-starts in pike *Esox lucius* using such an approach. This prediction is higher than any fish muscle power output measured to date.

The aim of the present study was to compare estimates of muscle power output from work-loop measurements on isolated fibres (both from this study and drawn from the

literature) with predictions made from whole-body swimming performance during fast-starts. The species used in this study were drawn from a range of habitat temperatures. It is known that increases in temperature correlate with increased muscle power output for a range of phyla (Stevenson and Josephson, 1990; Josephson, 1993). Greater muscle power availability should drive higher fast-start accelerations and thus higher velocities. We thus hypothesised that fast-start performance, in terms of velocity and acceleration, would be lower for colder species and that increases in fast-start performance would mirror increases in the muscle power available at higher temperatures. This study also set out to quantify the muscle kinetics for these starts to determine whether differences in fast-start performance were related to differences in muscle shortening.

## Materials and methods

### Fish

The marine fish *Notothenia coriiceps* (Nybelin), *Notothenia rossii* (Richardson), *Myoxocephalus scorpius* (L.), *Scorpaena notata* (L.), *Serranus cabrilla* (L.) and *Paracirrhites forsteri* (Bloch and Schneider) were used for this study. The Antarctic notothenioids were caught by the British Antarctic Survey around Signy Island, South Orkneys, in 1995; the short-horn sculpin *M. scorpius* were caught in St Andrews Bay, Scotland,

Table 1. Morphological body parameters of the fish used in this study

Species	<i>Paracirrhites forsteri</i>	<i>Serranus cabrilla</i>	<i>Scorpaena notata</i>	<i>Myoxocephalus scorpius</i>	<i>Notothenia rossii</i>	<i>Notothenia coriiceps</i>
<i>N</i>	6	5	7	7	5	4
<i>L</i> (m)	0.176±0.007	0.112±0.005	0.105±0.004	0.176±0.009	0.246±0.025	0.238±0.010
<i>m</i> (kg)	0.1076±0.0123	0.0202±0.0048	0.0231±0.0024	0.0929±0.0158	0.1578±0.0415	0.1585±0.0155
<i>m<sub>m</sub></i>	0.322, 0.424 ( <i>N</i> =2)	0.470 ( <i>N</i> =1)	0.363±0.008 ( <i>N</i> =4)	0.294, 0.301 ( <i>N</i> =2)	0.447±0.001 ( <i>N</i> =3)	0.300*
<i>S<sub>p</sub></i>	0.0886±0.0032	0.0948±0.0028	0.1195±0.0036	0.1402±0.0036	0.0861±0.0041	0.1032±0.0032
<i>S<sub>l</sub></i>	0.2120±0.0064	0.1781±0.0037	0.1895±0.0014	0.1252±0.0016	0.1432±0.0061	0.1566±0.0015
<i>S<sub>wet</sub></i>	0.4697±0.0123	0.4306±0.0058	0.4854±0.0074	0.4173±0.0048	0.3603±0.0146	0.4080±0.0054
<i>M</i>	0.0164±0.0008	0.0143±0.0003	0.0215±0.0008	0.0169±0.0004	0.0108±0.0007	0.0143±0.0005
<i>I<sub>1</sub>(S<sub>p</sub>)</i>	0.390±0.002	0.410±0.005	0.365±0.003	0.409±0.010	0.355±0.008	0.368±0.004
<i>I<sub>2</sub>(S<sub>p</sub>)</i>	0.444±0.001	0.472±0.005	0.434±0.005	0.473±0.012	0.419±0.009	0.427±0.006
<i>I<sub>1</sub>(S<sub>l</sub>)</i>	0.478±0.004	0.496±0.007	0.431±0.005	0.382±0.013	0.472±0.007	0.470±0.002
<i>I<sub>2</sub>(S<sub>l</sub>)</i>	0.545±0.004	0.563±0.007	0.495±0.006	0.445±0.014	0.540±0.007	0.540±0.002
<i>I<sub>1</sub>(S<sub>wet</sub>)</i>	0.452±0.004	0.466±0.005	0.406±0.003	0.397±0.003	0.428±0.005	0.430±0.002
<i>I<sub>2</sub>(S<sub>wet</sub>)</i>	0.518±0.004	0.534±0.005	0.471±0.004	0.463±0.004	0.498±0.006	0.498±0.003
<i>I<sub>1</sub>(M)</i>	0.380±0.001	0.405±0.004	0.343±0.004	0.335±0.003	0.349±0.007	0.357±0.004
<i>I<sub>2</sub>(M)</i>	0.422±0.001	0.459±0.005	0.390±0.004	0.381±0.003	0.401±0.009	0.409±0.005
<i>I<sub>1</sub>(m)</i>	0.372±0.004			0.344 ( <i>N</i> =1)	0.335±0.014	0.338 ( <i>N</i> =1)
<i>I<sub>2</sub>(m)</i>	0.418±0.004			0.388 ( <i>N</i> =1)	0.386±0.013	0.388 ( <i>N</i> =1)
<i>I(I)</i>	0.192±0.004	0.214±0.003	0.186±0.002	0.176 ( <i>N</i> =1)	0.190±0.004	0.197±0.005

Values are mean ± S.E.M., where *N* is the number of values unless indicated otherwise. Where *N*=1 or 2, one or both values are given.

See symbols list for definitions of parameters.

\*Data from Harrison *et al.* (1987).

UK, in 1995; the Mediterranean scorpionfish *Sc. notata* and comber *Se. cabrilla* were caught and supplied by the Zoological Station, Naples, Italy, in 1997; the tropical black-sided hawkfish *P. forsteri* were imported from the Hawaiian Islands in 1996. In their natural habitats, these fish experience the following temperature ranges: Signy Island, Antarctica ( $60^{\circ}43'S$ ,  $45^{\circ}36'W$ ),  $-2$  to  $1^{\circ}C$ ; North Sea,  $4$ – $17^{\circ}C$ ; Mediterranean Sea,  $10$ – $28^{\circ}C$ ; Hawaiian Islands,  $24$ – $26^{\circ}C$ . Temperature-controlled aquaria in our laboratory maintained the fish at their respective median temperature, i.e. *N. coriiceps* and *N. rossii* at  $0^{\circ}C$ , *M. scorpius* at  $15^{\circ}C$ , *Sc. notata* and *Se. cabrilla* at  $20^{\circ}C$  and *P. forsteri* at  $25^{\circ}C$ . The numbers and sizes of the fish can be found in Table 1. Fish were held at these temperatures for at least 4 weeks prior to observations and were fed daily on krill, chopped squid or shrimp.

#### Kinematic parameters

Fast-starts were filmed in a static tank with dimensions  $2.0 \times 0.6 \times 0.2$  m (length  $\times$  width  $\times$  height). The water temperature was controlled at the acclimation temperature for the species being filmed. Starts were elicited by visual or tactile stimuli; for *N. coriiceps* and *M. scorpius*, starts were elicited by a tap to the caudal peduncle with a rod, whilst the other species were startled by the rod approaching from the front. The tank was lit from underneath by a bank of five 70 W fluorescent strip lights. Overhead images of the fish were filmed via a mirror positioned at  $45^{\circ}$  above the tank. Fish silhouettes were recorded on 16 mm Ilford HP5 film on a NAC Inc., Japan, E-10 high-speed ciné camera at  $500 \text{ frames s}^{-1}$  using a 29 mm lens. The light path between the fish and the film was 2.6 m, and the frame diagonal was typically four fish lengths long. Film sequences were digitized on a NAC 160F film motion image analyser. The standard error of digitizing a reference point on sequential frames corresponded to 0.001 body lengths. Timing for the sequences was calibrated by means of a light strobing at 100 Hz within the camera. All fast-start sequences that did not show tilting or rolling of the fish were analysed.

The  $x, y$  coordinates of 10 equidistant points running from snout to tail along the spine were digitized by eye for each ciné frame. The centre of mass for a straight stretched fish lies at a distance  $\hat{l}_1(m)$  along the spine from the snout where  $\hat{l}_1(m)$  is the non-dimensional radius of the first moment of mass (see equation A14, Appendix). Using the procedures described in the Appendix (equations A30–A32), the  $x, y$  coordinates of this point on the spine were calculated. This 'quick' method was validated against a more rigorous method involving computation of the spine position from the fish outlines (equations A18–A29). Similarly, a detailed method is given in the Appendix for quantifying fish morphology. Validation of the various techniques is described more fully in a later section.

#### Velocity and acceleration

Velocity  $V$  and acceleration  $A$  were determined from the displacement of the centre of mass of the fish during the first complete tailbeat of each start. Fast-starts involve both

unsteady velocities and accelerations, and their estimates are very sensitive to the manner in which the data are smoothed. This study fitted cubic regressions to subsequent sections of the position data in order to smooth the estimates of position. This method is analogous to fitting a moving average (Webb, 1978; Frith and Blake, 1995; Harper and Blake, 1989, 1990; Domenici and Blake, 1991; Kasapi *et al.* 1992; Beddow *et al.* 1995; Franklin and Johnston, 1997) with the difference that we took a cubic fit where traditionally a linear fit has been used.

The position data gave a series of  $N$  values where there were  $N$  frames in the sequence. For each frame  $j$ , a 'smooth' estimate of the position was given by the value  $h(j)$ , where  $h(x)$  was the least-squares cubic regression for the  $x$  coordinates in frames  $j-n$  to  $j+n$  and the smooth width was  $2n+1$ . The velocity and acceleration for each frame were given by the first and second differentials, respectively, of  $h(j)$  with respect to time. Smoothed results were not calculated for the first and last  $n$  frames in the sequence. The procedure was repeated for the data in the  $y$  direction. Where there was a maximum or minimum to the data, then the cubic fit would accurately match the peak values. The smooth width was still important; if it was too small, then peak values would contain digitizing uncertainty, and if it was too large then it would encompass several peaks and thus be unable to give a good fit to each one.

The effect of the smooth width on the maximum velocity

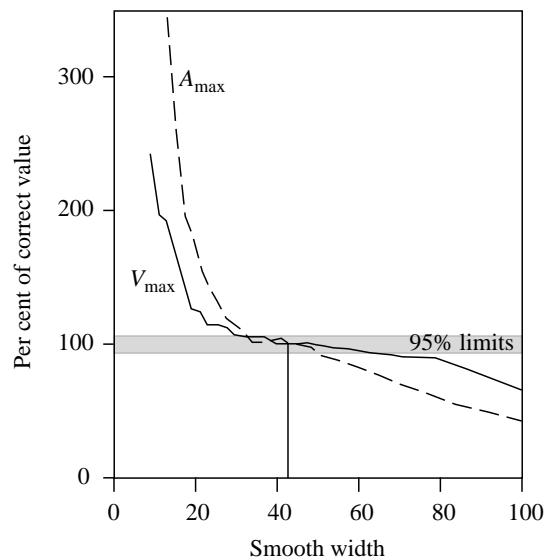


Fig. 1. Increasing the width of sequential portions of the cubic fit to the position data results in a decrease in the estimated maximum velocity  $V_{\max}$  and acceleration  $A_{\max}$ . The smooth width of 43 for this sequence (vertical line) results in a fit where the digitizing errors have been smoothed, but the overall displacement data are preserved. The standard error of the smoothed positions from the raw data is  $0.0015L$  ( $N=150$ ), where  $L$  is total length for this smooth width. The standard error of the position of a reference point digitized from sequential frames is  $0.00123L$  ( $N=80$ ). The smooth width of 43 can thus be justified from the digitizing accuracy. The 95 % confidence limits of the velocity and acceleration data are shown by the shaded region.

$V_{\max}$  and acceleration  $A_{\max}$  estimates can be seen in Fig. 1. As the smooth width increases, there is a sharp initial drop as the digitizing errors are smoothed. Next occurs a relatively level portion with the peaks and troughs being accurately fitted. Finally, the values of maximum velocity and acceleration decrease and the increasing smooth width causes over-smoothing. Values for the smooth width which gave accurate fitting of the maxima coincided with those that resulted in the standard error of the smoothed position data from the raw position data matching the standard error of repeatedly digitizing a point from the film (Fig. 1). Thus, we have confidence that the velocity and acceleration estimates were based on the correct degree of smoothing.

The correct value for the smooth width depends on the digitizing accuracy. The correct smooth width also depends on the number of digitized frames per tailbeat or similar event which produces a fluctuation in acceleration. Smooth width was estimated independently for each species analysed here.

Velocity and acceleration were determined for both the  $x$  and  $y$  directions, and the resultant was calculated as the total value. The acceleration estimate thus included the centripetal acceleration and did not necessarily take the same direction as the velocity. The tangential acceleration, which is the component of acceleration in the velocity direction, was also calculated. Rotational velocity and acceleration were estimated from the change in yaw angle in an analogous manner to the translational values, where yaw is the angle between the velocity vector and the spine at the position of the centre of mass  $\psi$  (see equation A33).

Length-specific velocity  $\hat{V}$  and acceleration  $\hat{A}$  were calculated relative to the total body length  $L$ , where  $\hat{V}=V/L$  and  $\hat{A}=A/L$ , respectively.

#### Power requirements during swimming

Fast-starts are rapid acceleration events, and during the start the useful power  $P_{\text{use}}$  expended to move in a tangential direction can be approximated by the inertial power  $P_{\text{iner}}$ , where:

$$P_{\text{use}} \approx P_{\text{iner}} = (m + m_a)VA \quad (1)$$

and  $m$  is the body mass,  $m_a$  is the added mass of water that must be accelerated with the body,  $V$  is the velocity, and  $A$  is the acceleration. The added mass of water that moves with a fish during fast-starts has been estimated as  $m_a=0.2m$  (Webb, 1982).

The inertial power as described in equation 1 is that required for linear accelerations. The inertial power required for a rotational acceleration  $P_{\text{iner,rot}}$  is given by a second relationship:

$$P_{\text{iner,rot}} = I\omega a, \quad (2)$$

where  $I$  is the moment of inertia of the fish [ $I=r^2(m+m_a)$ ] about the centre of rotation,  $\omega$  is the angular velocity,  $a$  is the angular acceleration, and  $r$  is the distance of the centre of mass of the fish from that centre of rotation. The tangential velocity  $V$  and

acceleration  $A$  are the following functions of the rotational values:  $\omega=V/r$  and  $a=A/r$ , respectively. Substituting the values for  $I$ ,  $\omega$  and  $a$  into equation 2 reduces the expression for  $P_{\text{iner,rot}}$  to the same as the translational inertial power  $P_{\text{iner}}$  as given in equation 1. Inertial power was thus calculated from tangential velocity and acceleration regardless of whether the fish followed a linear or turning course.

Translational inertial power estimates consider the acceleration of the centre of mass of the fish in the tangential direction. The centre of mass does not necessarily occur at a position along the spine; as a fish bends into a C-shape, the centre of mass moves away from the spine to lie within the space enclosed by the 'C'. Weihs (1973) showed the fish centre of mass in its actual position, moving away from the spine during bending. Later studies, however, take it to occur at the same point along the spine as in a straight-stretched fish. The position vector  $\mathbf{q}$  describing the true centre of mass is estimated by the mean position of 10 segments of the fish when each segment is given a weighting of its mass (volume):

$$\mathbf{q} = \frac{\sum_{i=1}^{10} \mathbf{s}(i)v_i}{M}. \quad (3)$$

$\mathbf{s}(i)$  is the position vector for the centre of each segment (see equations A30–A32),  $v_i$  is the volume for that segment as calculated for the straight fish (equation A9), and  $M$  is the total volume of the fish (equation A10). The effect of taking the actual centre of mass for the fish as opposed to that occurring along the spine can be seen in Fig. 2. Much of the initial movement of the spine occurs because the fish bends and does not represent a net displacement of the centre of mass. The course of the centre of mass is much straighter than that shown by the centre as positioned on the fish spine.

Useful hydrodynamic power  $P_{\text{use}} (\approx P_{\text{iner}})$  is expended to propel the fish in its direction of travel. However, as the body flexes, there is lateral motion; the total hydrodynamic power  $P_t$  is the total power expenditure during the movement both in the direction of travel and perpendicular to that direction. The hydrodynamic efficiency  $\eta$  is the ratio of the useful power to the total power:

$$\eta = \frac{P_{\text{iner}}}{P_t}. \quad (4)$$

Hydrodynamic efficiency has been estimated for a number of pike (*Esox lucius*) fast-starts by Frith and Blake (1995), who give values of  $\eta$  which relate  $P_t$  to useful hydrodynamic power and additionally give values of  $P_{\text{iner}}$  calculated for the same sequence. The mean  $\eta$  for the pike fast-starts which related  $P_{\text{iner}}$  to  $P_t$  is 0.31, and this value was used for the starts in the present study. Specific differences in kinematics may lead to specific differences in  $\eta$ ; however, this will only be resolved when detailed hydrodynamic analyses of fast-starts are applied to a range of species.

During swimming, the fish may rotate so that it does not face

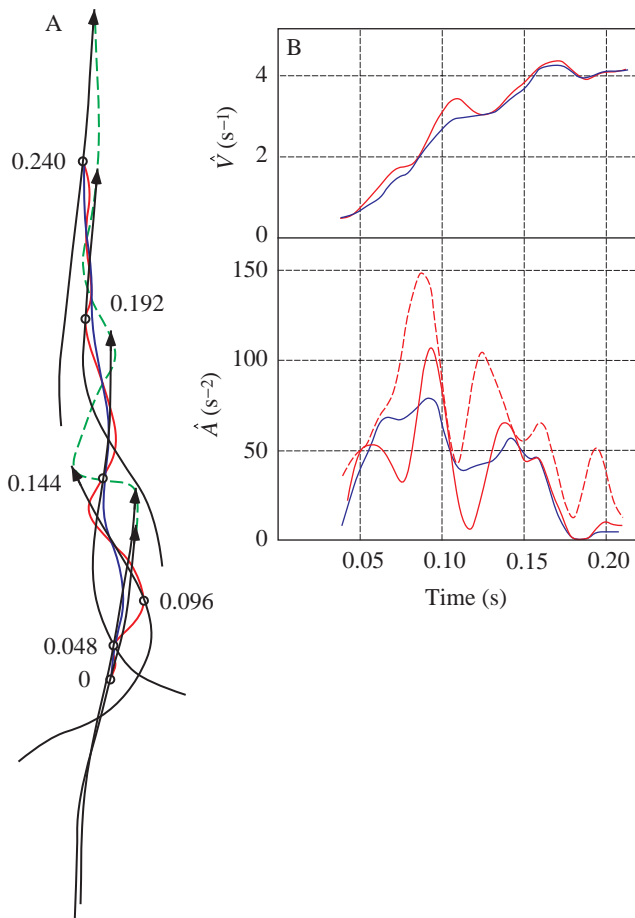


Fig. 2. (A) Spine positions for *Myoxocephalus scorpius*. Arrowheads indicate the snout, circles denote the position of the centre of mass as located on the spine, and numbers indicate the time (s) at which each image occurred. The solid blue line marks the displacement of the true centre of mass, the solid red line is the displacement of the centre of mass as located on the spine, and the dashed green line shows the displacement of the snout. (B) Non-dimensional velocity  $\hat{V}$  and acceleration  $\hat{A}$  estimates for the start shown in A. The blue lines are for the true centre of mass and the red lines for the centre as located on the spine. Solid lines are for tangential values, whereas the dashed line is the resultant of both tangential and centripetal acceleration.

its direction of travel. Yaw is taken as the angle between the velocity and the tangent to the spine at its centre of mass,  $\hat{l}_1(m)$ . Angular accelerations in yaw must be accompanied by turning torques, and the power for these can be calculated from equation 2, where  $I$  is the moment of inertia of the fish (equations A15–A17), and  $\omega$  and  $a$  are the angular velocity and acceleration, respectively, of the yaw. The moment of inertia is taken from straight-stretched bodies and so will be an overestimate for that from C-shaped postures. Nonetheless, the mean power expended for the yaw in 10 fast-start sequences was a mere 0.001 % of the inertial power expended for those starts. The costs of yawing were thus ignored during this analysis.

Mean inertial power was integrated for the duration of the

first complete muscle shortening cycle (as seen in the curvature plot, see Fig. 7). In almost all cases, the inertial power was positive. Negative inertial power did occasionally occur, corresponding to fish decelerations. However, assuming that such decelerations are passive during fast-starts, the mean power requirements were calculated solely from the positive contributions.

### Muscle strain

White muscle strain  $\epsilon_w$  and activation was measured directly in *N. rossii* and *P. forsteri* during fast-starts using the sonomicrometry and electromyography (EMG) method described by Franklin and Johnston (1997). Pairs of sonomicrometry crystals implanted into the myotomal muscle measure the muscle length from the velocity of sound transmission between the crystals. Anaesthesia was initiated with a 1:5000 (m/v) solution of bicarbonate-buffered MS222 (ethyl *m*-aminobenzoate) and maintained by irrigation of the gills with a 1:3 dilution of this solution during surgery. Surgery was performed in a constant-temperature room set to the acclimation temperature of the respective species. Sonomicrometry and EMG measurements were taken from superficial rostral fibres at  $0.35L$ , where  $L$  is the fish total length. For both species, previous dissections on dead specimens had confirmed that crystal positioning was in an alignment parallel to the surrounding fibres. Sonomicrometry data were also available for two other species recorded from our laboratory: *N. coriiceps* (Franklin and Johnston, 1997) and *M. scorpius* (G. Temple, unpublished data).

Muscle strain was predicted additionally from the shape and curvature of the body. The strain at the edge of the planform fish silhouette corresponds to the strain at the lateral line of the fish. This is the region where the red, aerobic fibres occur. Where muscle fibres run parallel to the spine, then their strain  $\epsilon$  can be calculated using trigonometry as:

$$\epsilon = \hat{b}\hat{c}, \quad (5)$$

where  $\hat{b}$  ( $=b/L$ ) is the length-specific distance from the spine to those fibres (half the width of the fish: see Appendix for methods of quantifying fish shape), and  $\hat{c}$  is the length-specific curvature of the spine at that location (equation A35). If the orientation of the red fibres is not parallel to the spine, then a correction should be made when calculating the strain (van Leeuwen *et al.* 1990) as oblique fibres undergo smaller strains than parallel fibres.

The white fibres run in a helical arrangement deeper within the fish than do the red fibres (Alexander, 1969). This helical arrangement results in the strain being similar for white fibres at different depths; however, this strain may be less than that for the adjacent red fibres. The gearing ratio is the ratio of the red fibre strain to the white fibre strain for a given curvature of the body and was predicted to take a value of approximately 4 (Alexander, 1969). In the present study, the gearing ratio  $\lambda$  was estimated as the ratio of the mean white fibre strain  $\bar{\epsilon}_w$  for a series of fast-starts (as measured using the sonomicrometry

technique) to the corresponding mean red fibre strain  $\bar{\epsilon}_{\text{red}}$  (as calculated by equation 5), where:

$$\lambda = \frac{\bar{\epsilon}_{\text{red}}}{\bar{\epsilon}_{\text{w}}} \quad (6)$$

Deviations in red fibre orientation from parallel to the spine are ignored. This results in a slight overestimate in the gearing ratio. However, this error is not propagated into estimates for the white muscle strain.

#### Validation of the techniques

A set of six *P. forsteri* fast-starts was used to validate the quicker method of digitizing the spine position 'by eye' against the full method involving equations A18–A29 in the Appendix. If the calculated spine position is considered to be correct, then the position judged by eye resulted in mean errors of 1.8 % and 1.5 % increase in  $\hat{V}_{\text{max}}$  and lateral line strain, respectively, and of 0.3 % and 1.1 % decrease in  $\hat{A}_{\text{max}}$  and  $\bar{P}_{\text{iner}}$ , respectively. The errors in velocity and acceleration, and therefore power, are smaller than those introduced by the smoothing technique (see Fig. 1), and so digitizing the spine by eye does not increase the uncertainty of the results. The errors for the strain estimates that are introduced by digitizing the spine by eye are similarly very small. If the mean white muscle strain  $\bar{\epsilon}_{\text{w}}$  is set by a mean gearing ratio from equation 6, then there will be no difference between  $\bar{\epsilon}_{\text{w}}$  for the two methods of estimating spine position. If the white muscle strain is set by an arbitrary gearing ratio, as has been the case for some other studies, then the difference between the two methods will be smaller than any error involved with the choice of gearing ratio.

#### In vitro muscle mechanics

Muscle contractile properties were determined for live fast fibre preparations from *Sc. notata* using the protocols described by Johnston *et al.* (1995), but with the following modifications. Preparations were isolated from the anterior abdominal muscles at a rostral position 0.35L along the fish. Fibres were dissected in a Ringer's solution with the following composition (in mmol l<sup>-1</sup>): NaCl, 143; sodium pyruvate, 10; KCl, 2.6; MgCl<sub>2</sub>, 1.0; NaHCO<sub>3</sub>, 6.18; NaH<sub>2</sub>PO<sub>4</sub>·2H<sub>2</sub>O, 3.2; Hepes sodium salt, 3.2; Hepes, 0.97; pH 7.3 at 20 °C. Both dissections and measurements were carried out at 20 °C. The length of the preparation was set to give maximal twitch. Preparations were frozen in isopentane cooled to -159 °C with liquid nitrogen. Frozen sections, 10 µm thick, were cut at several points along the preparation and stained for myosin ATPase activity (Johnston *et al.* 1974). Muscle mass was calculated from its volume (the product of length and cross-sectional area) assuming a density of 1060 kg m<sup>-3</sup> (Mendez and Keys, 1960).

Maximum contraction velocity  $V_0$  was determined using the slack test (Edman, 1979); fibres were given a step release during the plateau phase of an isometric tetanus sufficient to abolish force.  $V_0$  is the slope of the linear regression of step length against the time taken to redevelop force (6–8 step changes). Work-loop experiments were performed using single

sine waves. Cycle periods were tested in a range around 92 ms, the mean cycle period for the initial tailbeat as measured from ciné film. Fibre-length-specific peak-to-peak strain amplitude was set to 0.07, corresponding to that used by *M. scorpius* of similar size; the justification for this assumption is that the kinematics of these two species are similar (see Fig. 6). Two to three stimuli were given at a frequency of 260 Hz, which was shown to yield maximum tetanic force in preliminary experiments. Stimuli started just before peak length, with a duty cycle of 71.5–139.5°. The passive work done by unstimulated fibres was always less than 4 % of the total work and was subtracted from the total work in each case.

#### Statistics

Least-squares linear regression was performed on sets of data to test the dependence of each parameter on the predictor variable. The kinematic parameters describing velocity, acceleration and power were all heteroscedastic and so were only tested after logarithmic transformation. Reduced major axis (Model II) regression was performed where the predictor was a random variable (Rayner, 1985), i.e. the non-dimensional radius of the  $k$ th moment of volume  $\hat{l}_k(M)$  and  $P_{\text{iner}}$ .

A multivariate analysis of covariance tested the correlation between the kinematic parameters  $\hat{c}$ ,  $\epsilon_{\text{red}}$ ,  $\hat{U}$  and the fast-start performance parameters  $V_{\text{max}}$ ,  $\hat{V}_{\text{max}}$ ,  $A_{\text{max}}$ ,  $\hat{A}_{\text{max}}$  and  $P_{\text{iner}}$  with the habitat temperature as a factor, where  $\hat{U}$  is the length-specific velocity at which curvature travels along the body and  $\hat{V}_{\text{max}}$  and  $\hat{A}_{\text{max}}$  are the length-specific maximum velocity and acceleration of the fish, respectively. The fast-start performance parameters and  $\hat{U}$  were all log-transformed owing to their heteroscedastic nature.

Q<sub>10</sub> values were calculated from the slopes of least-squares linear regressions on log-transformed data for kinematic parameters and temperature. Q<sub>10</sub> values were calculated using the mean kinematic parameter for each and every species.

All statistical tests were considered significant at a 95 % confidence level.

## Results

#### Body morphologies

Length-specific fish chords are shown in Fig. 3. The various morphological parameters are given in Table 1 and shown in Figs 4 and 5 and provide a means to quantify differences between the shapes of the species. The non-dimensional radii of the moments of volume provide a good predictor of the non-dimensional radii of the moments of mass (Fig. 4). The non-dimensional radii of the moments of mass are predicted from the moments of volume by the following linear relationship:

$$\hat{l}_k(m) = 1.065\hat{l}_k(M) - 0.033, \quad (7)$$

where  $k$  takes a value of 1 or 2 for the first and second moments, respectively. The predicted radii of the moments of mass deviate from the relationship in equation 7 with a

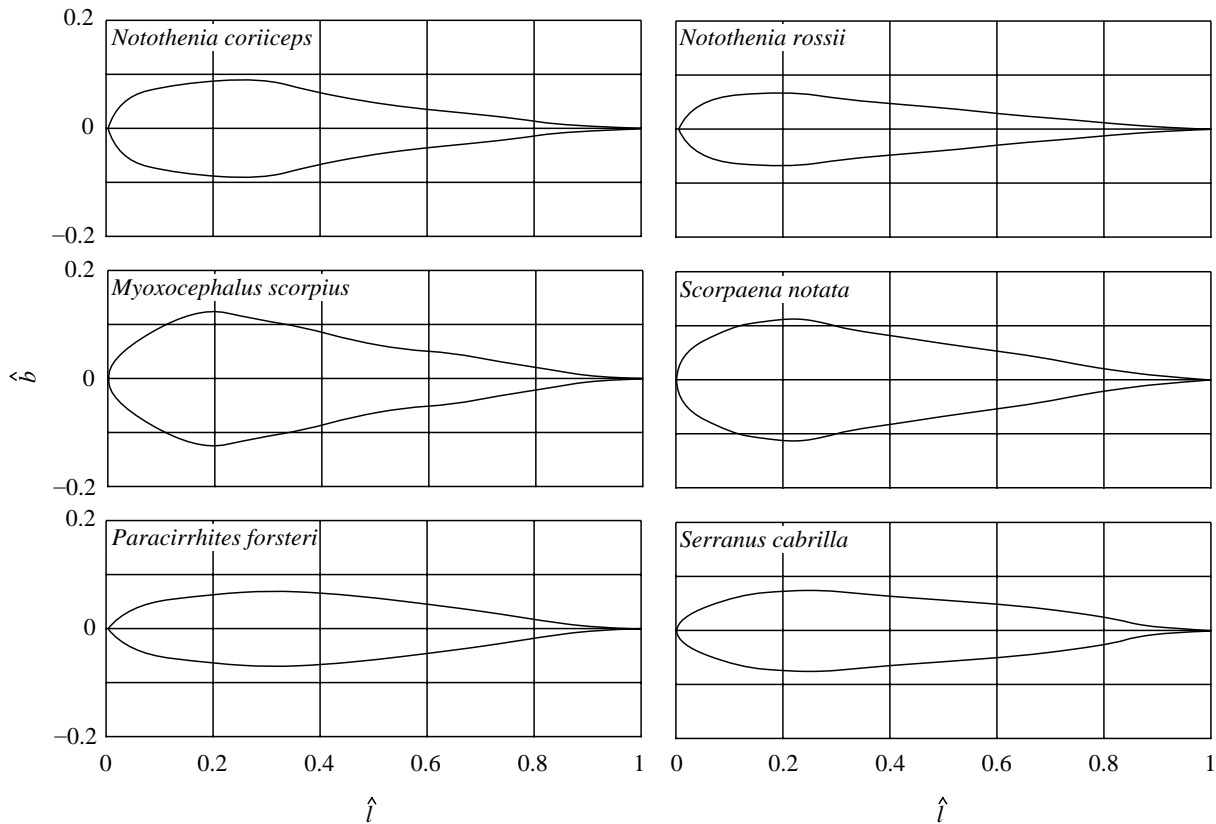


Fig. 3. Length-specific body chord  $\hat{b}$  as a function of the non-dimensional length  $\hat{l}$  for the six species in this study.

standard error of 0.0025 and with an error never more than 0.0207. Some of this variation is interspecific, with different species having different density distributions throughout their

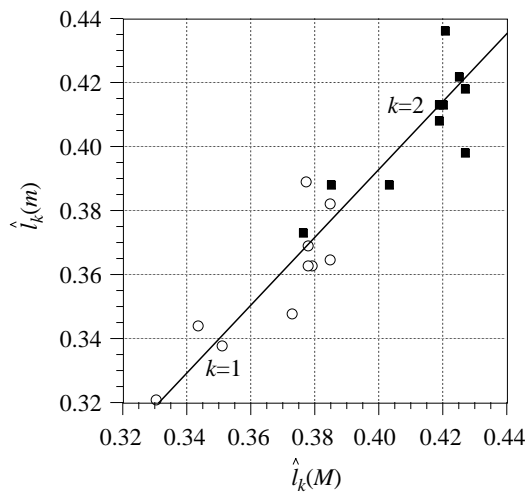


Fig. 4. The non-dimensional radii of the first and second moments of mass  $\hat{l}_k(m)$  are predicted by the non-dimensional radii of the first and second moments of volume  $\hat{l}_k(M)$ . Open circles,  $k=1$ ; filled squares  $k=2$ . The line denotes the reduced major axis regression of  $\hat{l}_k(m)$  on  $\hat{l}_k(M)$  (see text for explanation), with  $r^2=0.88$ ,  $P=0.0003$ . The volume distribution of the fish body can thus be used as an estimate of the mass distribution.

body. Nonetheless, the centres of mass for straight-stretched fish can be estimated reliably from the centres of volume as measured using two orthogonal views of the fish alone.

The relationships between the non-dimensional radii of the moments of area and volume are shown in Fig. 5. They are analogous to series given for the shapes of insect wings (Ellington, 1984). Relationships between the parameters have not been explained and have been termed 'laws of shape: rules that are obeyed even if the reasons for doing so are unknown' (Ellington, 1984). These relationships do, however, provide a good way to quantify body shape, and discrete clusters of points highlight specific morphologies (Fig. 5).

The mean depth to slenderness of each species is given by the ratio  $\hat{S}_l/\hat{S}_p$ , where  $\hat{S}_l$  and  $\hat{S}_p$  are the non-dimensional longitudinal and planform areas, respectively (see equations A1–A4). In general, *P. forsteri* is a deep, slender fish, while *M. scorpius* is the opposite extreme, wide and shallow. The non-dimensional radii of the moments of longitudinal area,  $\hat{l}_1(S_l)$  and  $\hat{l}_2(S_l)$ , show distinct groups for each species. The two species, *Sc. notata* and *M. scorpius*, have the greatest proportion of longitudinal area in their head region, with *M. scorpius* having the relatively deepest head. The length-specific estimate for the centre of mass  $\hat{l}_1(M)$  is similarly most anterior for these two species. *N. rossii* also has a low value for  $\hat{l}_1(M)$  because it has a relatively broad head, as shown by its low non-dimensional radii for the first and second moments of planform area  $\hat{l}_1(S_p)$  and  $\hat{l}_2(S_p)$ .

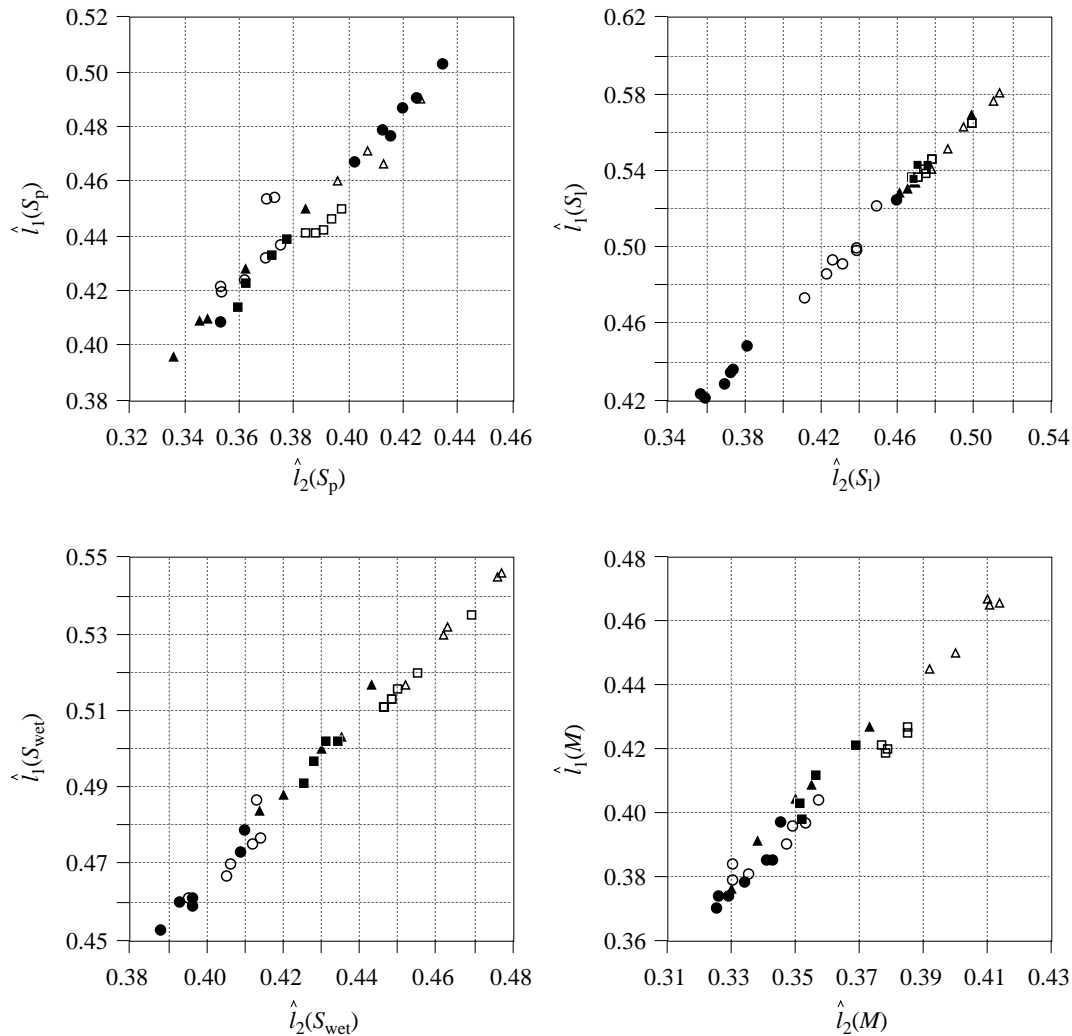


Fig. 5. Distributions of the non-dimensional radii of the first and second moments of planform area  $\hat{l}_k(S_p)$ , longitudinal area  $\hat{l}_k(S_l)$ , wetted area  $\hat{l}_k(S_{wet})$  and volume  $\hat{l}_k(M)$ . The reduced major axis coefficients of determination ( $r^2$ ) for these distributions are 0.93, >0.99, 0.99 and 0.97, respectively, with  $P < 0.0001$  for all the relationships. Symbols are as follows: open squares, *Paracirrhites forsteri*; open triangles, *Serranus cabrilla*; open circles, *Scorpaena notata*; filled circles, *Myoxocephalus scorpius*; filled triangles, *Notothenia rossii*; filled squares, *Notothenia coriiceps*.

There were no significant regressions between any of the mean morphological parameters and the habitat temperature, except one. The non-dimensional wetted area showed a significant positive regression with habitat temperature ( $r^2 = 0.686$ ,  $P = 0.0418$ ). However, wetted area affects viscous drag which, in turn, is a function of fish velocity. This study considers the initial moments of fast-starts where the velocity is low; therefore, the contribution of viscous drag is negligible and is ignored. For the purposes of this study, we will assume that habitat temperature has no significant effect on body morphology.

Fins are important for swimming, and their shape and area must be quantified for hydrodynamic analyses. However, such measurements are not required for the estimates of inertial power used in this study. Instead, this analysis concentrates on muscle action during swimming and so considers the shape of

the body which bounds the muscle. The non-dimensional muscle mass  $\hat{m}_m$  additionally is given in Table 1.

#### Fast-start muscle dynamics

A characteristic body motion was used by all the species during their fast-starts. This body motion can be described by the mean maximum curvature and strain values for the range of body positions, and these are shown in Fig. 6. The fish initially undergo a strong bending, resulting in a 'C' or an 'S' body shape. There was a continuum of shapes between these two extremes. Often a rapid bending of the central body was accompanied by an inertial lag of the tail, resulting in a very slight 'S' shape at the tail. Consequently, starts were not pigeon-holed into categories during this analysis, and all forms are considered together.

The initial bending occurred as a wave of bending travelling

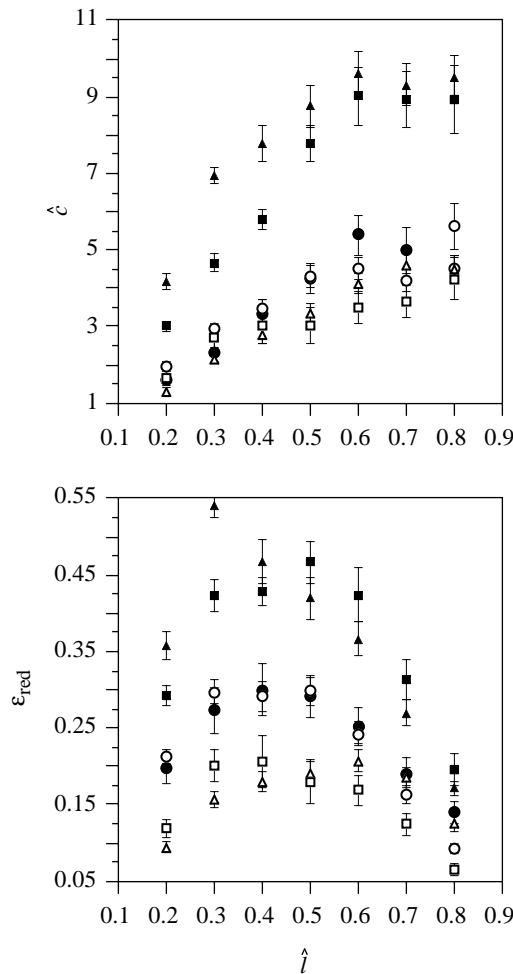


Fig. 6. The amplitude of the non-dimensional curvature  $\hat{c}$  increases with non-dimensional longitudinal body position  $\hat{l}$  during fast-starts. Peripheral strain  $\epsilon_{\text{red}}$ , in contrast, decreases from its maximum in the mid-fish towards the tail owing to decreasing chord length. Mean values for all the starts for each species are plotted  $\pm$  S.E.M. Symbols are as follows: open squares, *Paracirrhites forsteri* ( $N=14$ ); open triangles, *Serranus cabrilla* ( $N=36$ ); open circles, *Scorpaena notata* ( $N=38$ ); filled circles, *Myoxocephalus scorpius* ( $N=15$ ); filled triangles, *Notothenia rossii* ( $N=21$ ); filled squares, *Notothenia coriiceps* ( $N=27$ ).

from head to tail (Fig. 7) with length-specific velocity  $\hat{U}$ . Being a wave of bending, there are no discrete times when the fish is in a 'C' shape on either side. It is thus impossible to determine accurately the times for the classical stages of each start (Weihs, 1973). The cranium is a relatively rigid structure which does not bend significantly during the start. The tail, in contrast, is flexible and can bend considerably. The curvature thus increased along the fish to a position at approximately  $0.6L$ , where it then remained relatively constant (Fig. 6). All body parameters are considered in the range  $0.2-0.8L$ ; however, in some species, such as *M. scorpius*, the stiff cranium extends beyond the  $0.2L$  position and may influence the parameters at this location. In order to tidy subsequent plots (Fig. 7), the curvature and strain were set to decrease linearly

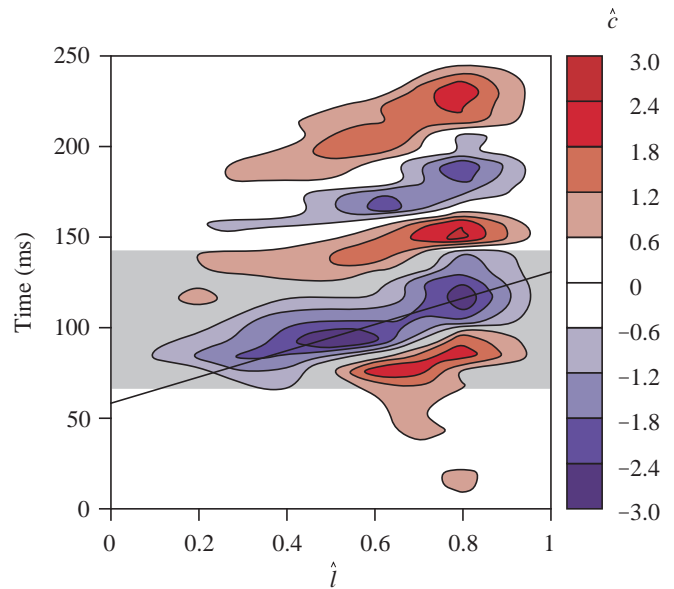


Fig. 7. Contour plot showing how the body curvature  $\hat{c}$  changes with both time and non-dimensional longitudinal position  $\hat{l}$  during a fast-start for *M. scorpius*. The slope of the solid line is inversely proportional to the rate at which the wave of curvature travels along the body ( $=1/\hat{U}$ ). The stippled area indicates the period over which the mean inertial power output was integrated, beginning at the first instance of body bending.

to zero between the extremes at  $0L$  and  $1L$  and the respective main body values at  $0.2L$  and  $0.8L$ .

The strain  $\epsilon_{\text{red}}$  is a function of both the local body chord and curvature. The chord decreases between  $0.2L$  and  $0.8L$  in all species, resulting in a general decrease in  $\epsilon_{\text{red}}$  (Fig. 6). All species except *N. rossii* showed a reasonably constant strain between  $0.3L$  and  $0.5L$ , where the increase in curvature balances the decrease in chord; their strains then decrease towards the tail. *N. rossii* showed a linear decrease in  $\epsilon_{\text{red}}$  from  $0.3L$  to the tail. Despite *M. scorpius* having the greatest length-specific chord (Fig. 3), it did not show the highest  $\epsilon_{\text{red}}$  because its body curvature was less than that of the notothenioids. Similarly, *P. forsteri* had the lowest mean  $\epsilon_{\text{red}}$  despite it being one of the most slender fish (as shown by  $\hat{S}_p$ ; Table 1). Body curvature thus has a greater effect on  $\epsilon_{\text{red}}$  than does body chord, and the strain at all positions along the fish increased with decreasing habitat temperature due to increasing curvature (Fig. 6).

Sonomicrometry data for fast-starts give mean white muscle peak-to-peak strains of  $0.10$ ,  $0.20$ ,  $0.10$  and  $0.12$  for *N. coriiceps* (Franklin and Johnston, 1997), *N. rossii* (Fig. 8), *P. forsteri* (this study) and *M. scorpius* (G. Temple, personal communication), respectively, at positions  $0.35L$ ,  $0.36L$ ,  $0.40L$  and  $0.35L$ , respectively. The gearing ratio  $\lambda$  is thus  $4.09$ ,  $2.49$ ,  $2.07$  and  $2.39$ , respectively, for *N. coriiceps*, *N. rossii*, *P. forsteri* and *M. scorpius* at these respective positions.

The predicted strain waves for each body position sometimes have broad peaks at maximum and minimum

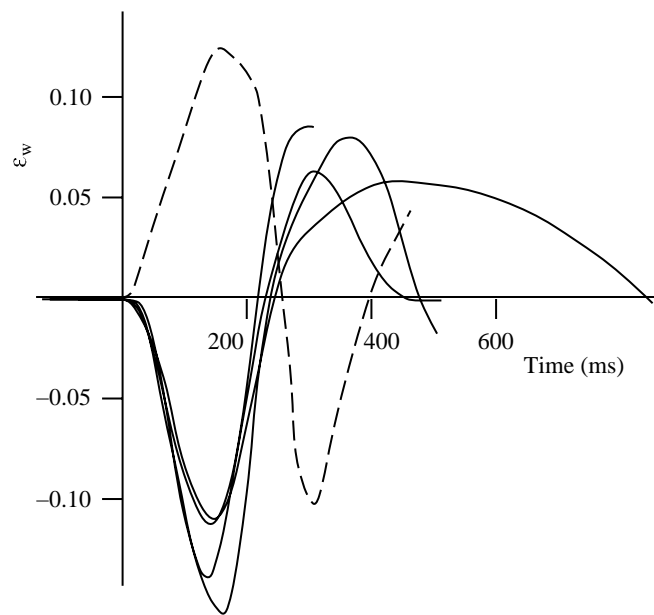


Fig. 8. Strains  $\epsilon_w$  in the rostral fast muscle fibres of one *N. rossii* individual for a series of fast-starts. Dashed and solid lines correspond to recordings from opposite sides of the body. Sonomicrometry crystals were positioned at a longitudinal position  $0.36L$  from the snout, where  $L$  is the total length.

muscle length. Measuring contraction duration as the period from maximum to minimum length will thus contain uncertainty as to the exact start and end of the contraction. An artificially low, but more robust, estimate for the contraction duration is the muscle strain divided by the maximum strain rate, and these durations range from 63 ms for the Antarctic fish to 25 ms for the Hawaiian and Mediterranean fish. Sonomicrometry traces show that these values are typically 0.57 of the actual shortening period. Mean contraction durations are longer in the Antarctic than in the warmer-water species and have a  $Q_{10}$  of 0.66. The mean contraction duration shows no significant regression with body position, i.e. contraction duration remains constant at all positions along the body. Caution should be used when comparing contraction durations between species because longer durations may reflect contraction over greater strains as well as contractions at slower rates.

In vitro muscle mechanics

The contractile properties for *Sc. notata* live fast fibres at 20 °C are summarised in Table 2. The maximum tetanic stress for *Sc. notata* of 239 kN m<sup>-2</sup> falls within the range of stress measured in other vertebrates i.e. from 241 kN m<sup>-2</sup> for the dogfish *Scyliorhinus canicula* (Curtin and Woledge, 1988) to 151 kN m<sup>-2</sup> in the saithe *Pollachius virens* (Altringham *et al.* 1993).

The maximum fibre length-specific contraction velocity  $V_0$  as measured by the slack test is 13.2 s<sup>-1</sup>. Maximum length-specific contraction velocities as measured both by slack-test

Table 2. Contractile properties for *Scorpaena notata* live rostral fast fibre preparations at 20 °C

Contraction type	Parameter	
Twitch	Maximum stress (kN m <sup>-2</sup> )	163.62±17.67
	Time to half-maximum force (ms)	9.32±0.73
	Time from maximum force to half-relaxation (ms)	10.05±0.36
Tetanus	Maximum stress (kN m <sup>-2</sup> )	239.18±16.72
	Time to half-maximum force (ms)	13.43±0.66
	Time from maximum force to half-relaxation (ms)	30.49±1.81
Slack test	Maximum length-specific contraction velocity, $V_0$ (s <sup>-1</sup> )	13.17±3.47 (N=4)
Work loop	Mean power output (W kg <sup>-1</sup> )	142.73±12.30

Mean ± S.E.M. (N=6 unless indicated otherwise).

methods and extrapolated from force-velocity relationships tend to increase with habitat temperature (Fig. 9) and  $V_0$  for *Sc. notata* falls within this range. The  $Q_{10}$  for maximum fish fast muscle length-specific contraction velocity is 2.2.

Fast-start performance

The different species showed characteristic styles of start. *M. scorpius* and *Se. cabrilla* typically swam off in a direction close to their original orientation, whereas the other species turned to a larger extent. During turning, there is a centripetal

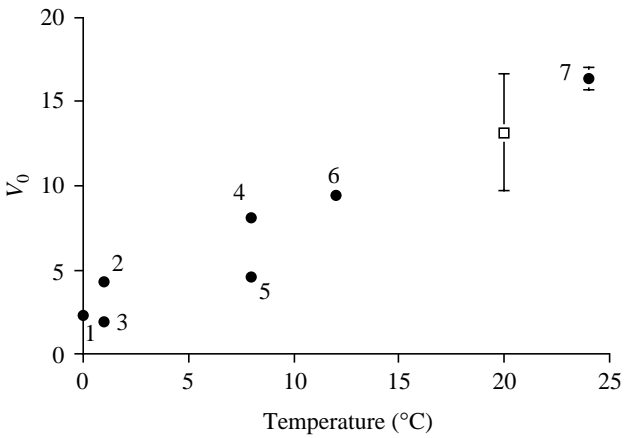


Fig. 9. Fish fast muscle length-specific contraction velocity  $V_0$  as measured by both slack test and force-velocity methods versus habitat temperature. The open square is for *Scorpaena notata* from this study. Filled circles denote data for *Notothenia coriiceps* (1, 2) (Franklin and Johnston, 1997; and Johnson and Johnston, 1991, respectively); *Trematomus lepidorhinus* (3), *Callionymus lyra* (4, 5) and *Thalassoma duperreyi* (7) (Johnson and Johnston, 1991); *Myoxocephalus scorpius* (6) (Langfield *et al.* 1989). Symbols denote mean values; error bars where shown are ± S.E.M., N=4.

Table 3. Kinematic parameters describing the first tail-beat of the fast-start

Species	<i>Paracirrhites forsteri</i> (N=23, n=3)	<i>Serranus cabrilla</i> (N=37, n=4)	<i>Scorpaena notata</i> (N=40, n=5)	<i>Myoxocephalus scorpius</i> (N=15, n=7)	<i>Notothenia rossii</i> (N=25, n=4)	<i>Notothenia coriiceps</i> (N=31, n=3)
Fast-start temperature (°C)	25	20	20	15	1	0
$\hat{U}$ (s <sup>-1</sup> )	13.57±1.96	24.45±1.21	17.73±0.91	11.42±1.03	5.17±0.43	4.17±0.23
$\hat{V}_{\max}$ (s <sup>-1</sup> )	7.47±0.72	13.15±0.95	10.22±0.55	6.55±0.64	3.16±0.29	2.72±0.13
$\hat{A}_{\max}$ (s <sup>-2</sup> )	143.72±14.79	273.81±17.05	223.72±10.96	97.53±6.35	45.91±4.69	39.49±1.82
$\hat{A}_{\max, \tan}$ (s <sup>-2</sup> )	120.81±14.23	259.75±16.89	193.18±10.86	91.79±6.37	38.81±3.94	34.77±1.95
$P_{\text{iner}}$ (W kg <sup>-1</sup> fish)	13.08±2.95	24.36±2.65	11.78±1.14	5.83±0.82	2.69±0.44	1.51±0.17
$L$ (m)	0.16±0.00	0.12±0.00	0.11±0.00	0.13±0.01	0.25±0.01	0.22±0.00
$V_{\max}$ (m s <sup>-1</sup> )	1.18±0.11	1.29±0.14	1.12±0.06	0.83±0.09	0.74±0.05	0.58±0.03
$A_{\max}$ (m s <sup>-2</sup> )	22.75±2.33	30.74±2.18	24.57±1.20	12.65±0.99	10.62±0.74	8.47±0.40
$A_{\max, \tan}$ (m s <sup>-2</sup> )	19.11±2.24	30.03±2.01	21.13±1.15	11.93±0.94	8.97±0.61	7.46±0.42
$P_t$ (W kg <sup>-1</sup> muscle)	124.26±29.53	167.18±18.16	104.69±10.14	62.69±8.82	19.44±3.15	16.19±1.82

Mean ± S.E.M.  $N$  = number of sequences analysed,  $n$ =number of individuals.

See symbols list for a full description of the parameters.

component of acceleration in addition to the tangential acceleration. The mean degree of turning can be quantified by the ratio of the maximum resultant acceleration to the maximum tangential acceleration and takes values of 1.05, 1.06, 1.14, 1.16, 1.18 and 1.20 for *Se. cabrilla*, *M. scorpius*, *N. coriiceps*, *Sc. notata*, *N. rossii* and *P. forsteri*, respectively. The different starting behaviours did not reflect the difference in methods for eliciting the starts. Comparisons of the fast-start performance between the species must be considered in the light of their different starting behaviours.

Values for the maximum length-specific velocity, acceleration and mean inertial power outputs achieved during the starts are given in Table 3. There are significant positive regressions between the habitat temperature and the maximum velocity, maximum acceleration and mean power output achieved during the fast-start. Maximum velocity and acceleration show a  $Q_{10}$  of 1.3 and 1.6, respectively (1.7 and 2.0 for the length-specific values). The mean estimated muscle-mass-specific power requirement shows a  $Q_{10}$  of 2.5. This value is less than the  $Q_{10}$  of 3.1 from the work-loop studies shown in Fig. 11; however, a  $t$ -test showed no significant difference between these values. Inertial power output is the product of velocity and acceleration; the recorded values of  $V_{\max}$  and  $A_{\max}$  are maxima, but they provide a good indication as to the mean velocity and accelerations during the first tailbeat. Maximum fast-start velocity and acceleration should therefore be related to the square root of the power available from the muscles, thus explaining their smaller change with temperature than for  $P_{\text{iner}}$ . Inertial power output is, in turn, related to the maximum contraction velocity of the muscle fibres.

#### Control of fast-starts

Fish swam with a range of fast-start performances, as measured by their velocity, accelerations and power outputs (Table 3). A multivariate analysis of covariance (MANCOVA)

on the pooled data showed that temperature had a significant effect on the variation in the fast-start parameters. Table 4 shows the significance levels for a series of univariate  $F$ -tests from the MANCOVA:  $\hat{U}$  and contraction duration show the strongest correlations with fast-start parameters, and muscle strain  $\epsilon_{\text{red}}$  is also important; however, the body curvature  $\hat{c}$  does not show any significant correlations with the fast-start parameters.

It is interesting to note that the phase of the contraction waves between muscle fibres along the body is a more reliable predictor of fast-start performance than the strain or strain rate used by any one particular fibre. Correlations between an individual muscle's contractile properties and whole-animal swimming performance should thus be used with caution.

## Discussion

### Fast-start kinematics

Fish fast-starts involve a wave of curvature that travels posteriorly along the spine. This wave is analogous to the wave of curvature during steady swimming (Gray, 1933). As the

Table 4. Univariate  $F$ -tests with  $d.f.=4,114$  from the multivariate analysis of covariance

Covariates	Dependent variable				
	$V$	$\hat{V}$	$A$	$\hat{A}$	$P_t$
$\hat{c}$	0.313	0.456	0.457	0.743	0.312
$\epsilon_{\text{red}}$	0.013	0.004	0.010	0.004	0.028
$\hat{U}$	<0.001	<0.001	<0.001	<0.001	<0.001
Contraction duration	<0.001	<0.001	<0.001	<0.001	<0.001

Values are the probabilities that there is no correlation between the dependent variable and the covariate.

body does not flex simultaneously at all positions, it is difficult to categorise a start into discrete stages. Weihs (1973) described fast-starts as consisting of three discrete stages, and Webb (1978) categorised starts into forming initial 'C' or 'S' shapes. However, body flexion varies with both longitudinal position and time, and so there are no discrete moments when the fish is bent evenly into any particular shape; the starts in the present study achieved a range of body shapes between the classical 'C' and 'S' shapes. A further problem may be encountered when measuring the tailbeat amplitude for a starting fish which swims on a curved trajectory. Tailbeat amplitude has traditionally been measured as the lateral displacement of the tail from the direction of travel (e.g. Bainbridge, 1958; Videler and Hess, 1984), but swimming on unsteady courses raises uncertainty as to the reference direction. Additionally, yaw of the fish body away from its instantaneous direction will add further discrepancies between a measured tailbeat amplitude and the actual body shape. Quantifying fast-starts by the degree of curvature achieved at the various longitudinal positions has made it possible to compare all starts regardless of the body shapes involved and the course swam.

Fast-start performance is linked strongly to the velocity  $\hat{U}$  at which the curvature wave travels along the spine (Table 4). The ratio  $\hat{V}_{\max}/\hat{U}$  is similar to the slippage ratio  $\hat{V}/\hat{U}$  for steady swimming, which has been used as an indicator of hydrodynamic efficiency (Videler and Hess, 1984). The mean  $\hat{V}_{\max}/\hat{U}$  takes values from 0.54 for *P. forsteri* to 0.68 for *N. coriiceps*. Indeed, there is a significant negative regression between the slippage ratio  $\hat{V}_{\max}/\hat{U}$  and habitat temperature ( $r^2=0.822$ ,  $P=0.0126$ ), with higher slippage ratios occurring at lower temperatures. Slippage ratios for steady swimming are the ratio of  $\hat{U}$  to the mean swimming velocity and so would tend to take values greater than this ratio of  $\hat{V}_{\max}/\hat{U}$ . Data reviewed by Videler (1993; his Table 6.1) show a slippage ratio of  $0.733 \pm 0.013$  (mean  $\pm$  S.E.M.) for the steady swimming of 14 species. The slippage ratios during the fast-starts in this study are thus comparable to that in steady swimming, showing an impressive effectiveness of the motion even during the initial moments of the start.

Each fish is able to modulate its fast-start performance by varying  $\hat{U}$ , as shown for *Se. cabrilla* in Fig. 10. There has been some debate as to whether fast-starts are controlled by simultaneous muscle activation to all myotomes or by a wave of muscle activation. Jayne and Lauder (1993) measured the onset of EMG activity to be synchronous at different longitudinal positions for the bluegill sunfish *Lepomis macrochirus*; however, they measured a posterior propagation of EMG activity during burst-and-glide swimming in the largemouth bass *Micropterus salmoides* (Jayne and Lauder, 1995b). If fast-starts were initiated by simultaneous EMG activity in all myotomes, then modulation of  $\hat{U}$  would not be possible by a change of timing of the activation between myotomes. The slowest mean  $\hat{U}$  is  $4.17 \text{ s}^{-1}$  for *N. coriiceps*, resulting in a 120 ms delay for the maximum curvature to travel between  $0.3L$  and  $0.8L$ ; it is inconceivable that such a delay

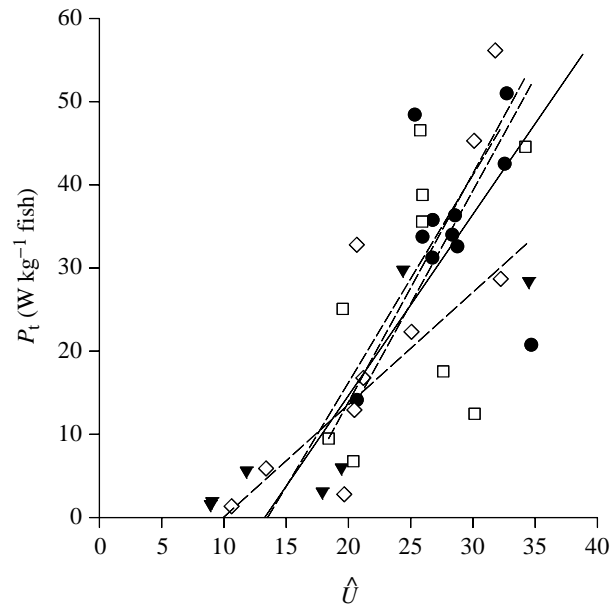


Fig. 10. Reduced major axis analysis showed that there was a significant positive regression between the total power requirement  $P_t$  and the length-specific velocity of the wave of curvature along the body  $\hat{U}$  for each *Serranus cabrilla* individual. The solid line denotes the regression for the pooled data ( $r^2=0.41$ ,  $P<0.0001$ ). Each individual is denoted by a different symbol and dashed regression line. For all individual regressions,  $P<0.01$ .

can occur as a result of modulatable differences in muscle kinetics along the fish. Indeed, for burst-and-glide swimming, Jayne and Lauder (1995b) found that as the velocity increased the rate of posterior propagation of EMG activity in the deep myomeric muscle also increased. We conclude that the wave of muscle contraction, and hence body curvature, along the fish occurs in part as the result of a posteriorly travelling wave of EMG activity during fast-starts.

#### Muscle geometry and mechanics

The link between white fibre strain and the adjacent red fibre strain has been treated differently every time it has been considered. Rome *et al.* (1988) estimated the white fibre strain in carp *Cyprinus carpio* by using a gearing ratio of 4 (following the reasoning of Alexander, 1969) and estimating red fibre strain using a form of equation 5. Rome and Sosnicki (1991) measured the sarcomere lengths of frozen carp that had gone into rigor. They found that the red fibre strain varied as a function of both the curvature of the spine and the distance of the fibres from the spine. Their white fibre strain varied only as a function of spine curvature. However, these fibres did show significant changes in length between the rigor and post-rigor state. The gearing ratio was found to be 4.25, 2.76 and 1.62 for anterior, middle and posterior regions of the carp, respectively. van Leeuwen *et al.* (1990) estimated red muscle strain in carp using corrections for fibre orientation. They then calculated white fibre strain by using a gearing ratio of 2. These carp data (van Leeuwen *et al.*

1990) were later reanalysed taking a new gearing ratio of 4 (van Leeuwen, 1992).

Fibre orientation changes from a helical geometry in the bulk of the body (Alexander, 1969) to being more parallel to the spine at the caudal peduncle. This change should cause a corresponding change in gearing ratio. In the extreme case, the mean gearing ratio across the fish should approach 2 in the caudal peduncle, and this has been measured in carp (Rome and Sosnicki, 1991). If the gearing ratio does drop to its minimum value of 2 in the caudal myotomes, then the varying muscle geometry along the fish coupled to the specific curvatures employed by these fast-starts would result in the strains and strain rates being similar between the different myotomes (see Fig. 6). Indeed, sonomicrometry measurements have shown the white fibre strain amplitude during fast-starts to be similar at rostral (0.35L) and caudal (0.65L) sites for *N. coriiceps* (Franklin and Johnston, 1997); similarly, estimates of red muscle strain in carp have shown that, during steady swimming, the change in fish width can exactly compensate for an increasing body curvature to result in similar strains at all positions (van Leeuwen, 1992). If, however, the gearing ratio does not drop to its minimum value of 2, then the strain and strain rate would show a decrease towards the caudal myotomes, resulting in a lower mass-specific power output in this region and a potential for greater force production. The accuracy of the white fibre strain estimates is almost certainly limited by the choice of the gearing ratio. Understanding the functions of different muscles during fast-starts clearly requires information on both muscle structures and geometries along the length of the body as well as detailed kinematic measurements of the body motions.

The fast-starts analysed may not have been at maximum performance and, by definition, they will never have exceeded the maximum possible performance. Therefore, estimates of the mean fast-start power output will necessarily be underestimates of the maximum mechanical power possible from the muscles. Indeed, the estimated muscle-mass-specific total power output of  $104.7 \text{ W kg}^{-1}$  for *Sc. notata* at  $20^\circ\text{C}$  (Table 3) is lower than its measured maximum power available of  $142.7 \text{ W kg}^{-1}$  (Table 2). This measured muscle power output for *Sc. notata* is the highest yet measured for a vertebrate muscle and even exceeds the  $135 \text{ W kg}^{-1}$  measured at  $35^\circ\text{C}$  for the lizard *Dipsosaurus dorsalis* (Swoap *et al.* 1993) and the  $107.2 \text{ W kg}^{-1}$  for the mouse also at  $35^\circ\text{C}$  (James *et al.* 1995).

#### Temperature effect on fast-starts

Comparisons of maximum length-specific swimming velocities among the species studied are complicated by differences in body length (Tables 1, 3). Unfortunately, the scaling exponents of  $\hat{V}_{\max}$  are not known for the majority of the species studied. Data in the literature suggest that scaling exponents for  $\hat{V}_{\max}$  vary between species and with the thermal acclimation state of the individual (Temple and Johnston, 1998). It is therefore not advisable to correct  $\hat{V}_{\max}$  to a standard body length using generalised scaling exponents. Nonetheless,

a general trend across all species is that absolute velocities increase whereas length-specific values decrease with increasing fish length (Domenici and Blake, 1997). Despite these opposing scaling relationships between  $V$  and  $\hat{V}$  with  $L$ , the data from the present study show an increase in both  $V$  and  $\hat{V}$  with increasing temperature. There is thus an increase in fast-start performance due to temperature irrespective of any scaling effects.

Differences in  $\hat{V}_{\max}$  may be expected between distantly related species (Garland and Adolph, 1994). Phylogenetically based comparisons of individuals of identical length would be required to ascertain evolutionary adjustments in  $\hat{V}_{\max}$  between species living at different habitat temperatures (Huey, 1987; Harvey and Pagel, 1991). An interesting observation in the present study was that the Antarctic species *N. rossii* and *N. coriiceps* flexed their bodies with greater curvature than did the temperate and tropical fish. Comparisons among Notothenidae from Antarctica and from the coast of South America would provide an insight into whether such differences in swimming behaviour were associated with some specific adaptation to low temperatures.

Studies with single skinned muscle fibres (Johnston, 1990) and bundles of live muscle fibres (Johnson and Johnston, 1991) from 20 fish species representing 13 different families show the following patterns: maximum unloaded shortening velocity is positively correlated with mean habitat temperature (see also Fig. 9), whereas maximum force generation falls in the range  $160\text{--}250 \text{ kN m}^{-2}$ . Rates of muscle relaxation are also significantly faster for tropical than for cold-water species at their normal body temperature (Johnson and Johnston, 1991). Power output from a muscle, which is the product of force and shortening velocity, should therefore be correlated with body temperature, a conclusion that holds for work-loop studies in a range of invertebrate and vertebrate species (Stevenson and Josephson, 1990). The relationship between muscle power output and habitat temperature, both measured from work loops and predicted from swimming, for the fast-starts in the present study also fits into this general pattern (Fig. 11). Although quantitative conclusions must await phylogenetically based studies, it would seem that muscle power output decreases at lower temperatures and this in turn limits the fast-start performance of cold-water species.

#### Conclusions

Fast-starts occur as waves of curvature travelling along the fish body in a manner analogous to steady swimming. Curvature increases in amplitude towards the tail.

The gearing ratio between the red and white muscle strains varies between species for the rostral myotomes.

Increases in median habitat temperature correlate with an increase in the velocity of the wave of curvature along the fish and a decrease in body curvature, peripheral strain and the contraction duration.

Fast-start performance in terms of fish velocity, acceleration and power output correlates more strongly with the velocity at which the wave of curvature passes along the body than with

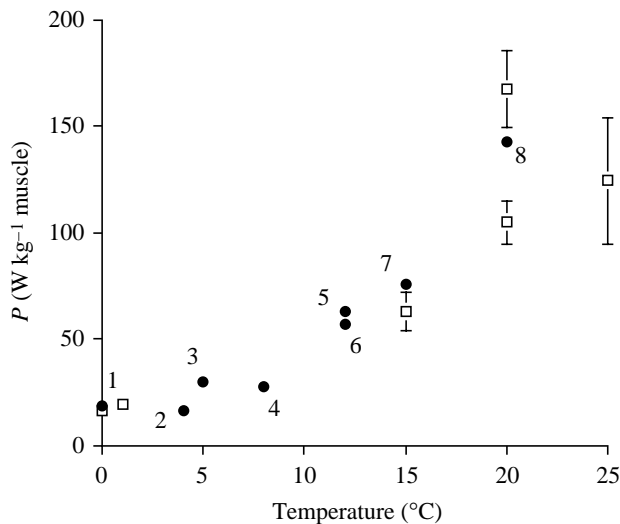


Fig. 11. Fish muscle-mass-specific power output as a function of habitat temperature. Open squares are the values of  $P_t$  predicted from the fast-starts in this study. The mean values from all the starts for each species are plotted  $\pm$  S.E.M. The filled circles are data from work-loop experiments: *Notothenia coriiceps* (1) (Franklin and Johnston, 1997); *Gadhus morhua* (2, 4) (Moon *et al.* 1991; Anderson and Johnston, 1992), respectively; *Myoxocephalus scorpius* (3, 6, 7) (Altringham and Johnston, 1990; James and Johnston, 1998; G. Temple, personal communication, respectively); *Pollachius virens* (5) (Altringham *et al.* 1993); *Scorpaena notata* (8) (this study).

the curvature or muscle kinetic properties at any one site along the body. Whole-body performance is thus determined by the concerted action of all the myotomes within the body.

Muscle power output increases with increasing median habitat temperature for the species studied. The initial hydrodynamic power output during the start is proportional to the product of the velocity and acceleration. Therefore, neither velocity nor acceleration is directly proportional to the muscle power output, and thus to the strain rate, during the initial stages of the start. Rather, velocity and acceleration are proportional to the square root of the power. This can be seen from the  $Q_{10}$  values for velocity (1.3), acceleration (1.6) and power (2.5).

Fast-start performance is limited by the power available from the muscles; this, in turn, is limited by muscle performance at different temperatures. Antarctic fish muscle delivers lower power output than does temperate and tropical fish muscle, and this results in their having the lowest fast-start performance.

### Appendix

Kinematic analyses of fish swimming face the problem of resolving two classes of motion: changes in body shape and changes in body position. Shape changes are caused by the action of the axial muscles stretching and contracting on opposite sides of the body. Information on body shape can thus be used to estimate muscle strain along the body. Changes in

the position of the centre of mass can be used to estimate swimming velocities and accelerations.

When viewed from above, the centre of mass of a straight-stretched fish lies on the spine. During fast-starts, fish can undergo substantial bending, and in such cases the centre of mass moves away from the spine. If the centre of mass is assumed to lie on the spine, then the velocity and acceleration estimates will include a component, due to the bending of the fish, that is not a reflection of the forward motion of the fish.

This Appendix outlines a method that resolves fish motion into its components of changing body shape and body position. The method requires information on the mass distribution along the fish, which is dealt with in the first four sections.

### Morphology measurements

Parameters describing fish mass can be determined from a pair of orthogonal images of the fish. Such images are not invasive, are quick to capture and can be taken either from live fish or from those needed fresh and intact for other experiments. For cases where density is homogeneous throughout the body, the distribution of volume mimics the distribution of mass. Thus, the moments of mass and the radii describing these moments are approximated by the moments and radii of the volume distribution.

Longitudinal and planform images only give information about the depth and width of the fish; they will not describe the shape of each transverse section. In this analysis, the fish is assumed to have an elliptical profile in transverse section. As shown by the results, the predicted volume distribution gives a close match to the mass distribution, and this assumption is therefore justified for the species examined here.

### Shape parameters

Planform and longitudinal images of freshly killed fish bodies were captured using a JVC TK-1281 video camera, printed with a Sony UP-3000P video printer and then scanned into a Power Macintosh computer. The total length  $L$  of the fish was measured using a reference object also captured by the camera. NIH Image version 1.24 software was used to superimpose a grid of 51 equally spaced parallel lines onto the fish outlines with the lines perpendicular to the longitudinal axis of the fish. The coordinates of the intersections of the grid with the fish outlines were digitized and represent the corners of 50 adjacent parallelograms that fit within each image.

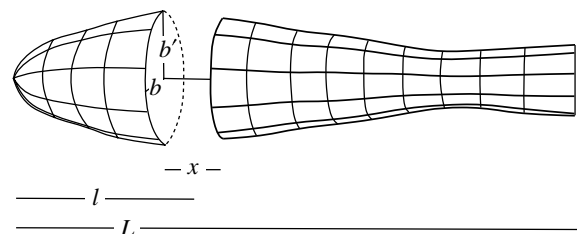


Fig. 12. Each fish segment has width  $2b$ , depth  $2b'$ , thickness  $x$ , and has its centre  $l/L$  body lengths from the snout.

The body outlines were taken to include the open tail but with the other median and appendicular fins flat on the body; this is all that is required to calculate the mass distribution along the fish. For more detailed hydrodynamic analyses, where the added mass of the fish at all longitudinal positions is required, then the median fins should be extended.

The fish has width  $2b$  and depth  $2b'$ , and each segment (parallelogram) has a length  $x$  in the longitudinal direction (Fig. 12). The area  $s_i$  for each segment is thus approximated by:

$$\text{planform area,} \quad s_{p,i} = 2b_i x, \quad (\text{A1})$$

$$\text{longitudinal area,} \quad s_{l,i} = 2b'_i x, \quad (\text{A2})$$

$$\text{wetted area,} \quad s_{\text{wet},i} = \pi(b_i + b'_i)x. \quad (\text{A3})$$

The total area  $S$  for the fish is thus:

$$S = \sum_{i=1}^{50} s_i. \quad (\text{A4})$$

The longitudinal distance of the centre of each segment from the snout is  $l_i$  and the  $k$ th moment of area about the snout is:

$$S_k = \sum_{i=1}^{50} s_i l_i^k. \quad (\text{A5})$$

For comparative purposes, length and areas can be non-dimensionalised by the fish length  $L$  to give:

$$\hat{l}_i = \frac{l_i}{L}, \quad (\text{A6})$$

$$\hat{S}_1 = \frac{S_1}{L^2}, \quad \hat{S}_p = \frac{S_p}{L^2}, \quad \hat{S}_{\text{wet}} = \frac{S_{\text{wet}}}{L^2}. \quad (\text{A7})$$

The non-dimensional radius of the  $k$ th moment of area about the snout is thus:

$$\hat{l}_k(S) = \left( \frac{S_k}{SL^k} \right)^{1/k}. \quad (\text{A8})$$

#### Volume parameters

The volume of each segment  $v_i$ , as measured from the fish outlines, is:

$$v_i = \pi b_i b'_i x, \quad (\text{A9})$$

and thus the total volume  $M$  of the fish is:

$$M = \sum_{i=1}^{50} v_i. \quad (\text{A10})$$

The  $k$ th moment of the volume about the snout is:

$$M_k = \sum_{i=1}^{50} v_i l_i^k, \quad (\text{A11})$$

and non-dimensional values for volume and the radius of the  $k$ th moment of area from the snout are:

$$\hat{M} = \frac{M}{L^3} \quad \text{and} \quad \hat{l}_k(M) = \left( \frac{M_k}{ML^k} \right)^{1/k}, \quad (\text{A12})$$

respectively.

#### Mass parameters

The body mass  $m$  of freshly killed fish was measured on a Mettler PE3000 balance. Fish were frozen, partially thawed and then placed on a square grid with their longitudinal axis parallel to one of the axes of the grid. Approximately 10 transverse sections were cut along the fish; the length of each section was measured with Vernier calipers and the mass  $m_i$  measured to the nearest 0.1 g. White myotomal muscle, as judged by its colour, was dissected from each section and weighed separately; i.e. the minor portion of lateral red muscle was excluded from this measurement. The non-dimensional muscle mass  $\hat{m}_m$  is the proportion of white myotomal muscle to total body mass. A mass loss of  $2.0 \pm 0.3\%$  (mean  $\pm$  S.E.M.) occurred during the cutting procedure. The mass of each section was thus increased by the factor  $m/\sum m_i$  to compensate for this loss. The centre of mass for each section was assumed to lie half-way along the section and was at a distance  $l_i$  from the snout.

The  $k$ th moment of mass  $m_k$  is:

$$m_k = \sum_{i=1}^n m_i l_i^k, \quad (\text{A13})$$

where  $n$  is the number of sections cut.

The non-dimensional radius of  $m_k$  from the snout is:

$$\hat{l}_k(m) = \left( \frac{m_k}{mL^k} \right)^{1/k}. \quad (\text{A14})$$

The centre of mass for a straight-stretched fish lies at a radius of  $\hat{l}_1(m)$  from the snout. Where mass measurements of the fish segments were not available, they were estimated from the volume distribution. This approximation makes the simplifying assumptions that the densities of the various segments are equal and also that fish bodies are elliptical in cross section. Nonetheless, the linear regression coefficient for  $\hat{l}_k(m)$  against  $\hat{l}_k(M)$  was  $r^2=0.88$  (Fig. 4), and so 88% of the fish mass distribution can be explained by these simple approximations.

The moment of inertia  $I$  about the centre of mass of the fish was determined using a compound pendulum technique. A long hypodermic needle was placed transversely through the midline of a frozen fish, near its tail. The needle, and thus the fish, was balanced on two parallel metal edges, and the fish swung like a pendulum. The moment of inertia for the needle is negligible compared with that of the fish. The fish moment of inertia  $I$  is thus given by:

$$I = \frac{rmgt^2}{4\pi^2}, \quad (\text{A15})$$

where  $r$  is the distance of the centre of mass from the pendulum axis (needle),  $g$  is gravitational acceleration, and  $t$  is the period of oscillation. The moment of inertia can be estimated independently from the volume distribution by:

$$I = \frac{m}{M} \sum_{i=1}^{50} v_i [l_i - l_1(M)]^2. \quad (\text{A16})$$

The non-dimensional radius of the moment of inertia from the centre of mass is:

$$\hat{l}(I) = \left( \frac{I}{L^2 m} \right)^{1/2}. \quad (\text{A17})$$

#### *Locating the spine in a fish*

Locating the spine position is an important aspect of resolving body shape from fish position. Spine curvature can be used to derive local axial muscle strain using procedures described in the Materials and methods section of the present study. Furthermore, the centre of mass can be estimated by taking a weighted mean of the spine positions for a series of sections along the fish where the weighting is the mass of each section.

The spine position can be modelled to divide the fish with equal volumes, areas or distances between its two sides. There are reasons why each possibility should be considered. Fish tissue can be considered relatively incompressible: its

volume remains relatively constant, and so if it changes length in one dimension it must also change length in others. The spine length may also be reasonably constant. When a bend pushes one side of the fish into compression, then that side will get wider and deeper to maintain a constant volume on that side of the fish. However, the opposite side must get narrower and shallower to maintain a constant volume. Such a hypothesis involves the fish having a different depth on both sides of the spine so that a sheet that runs vertically through the spine in a straight fish, would thus curl towards the narrower side during bending. The depth of the fish may alternatively remain constant; this would keep the sheet through the spine vertical during bending. During bending, the side in compression must get wider to maintain a constant area of tissue on that side of the fish whilst the opposite side gets narrower; the spine can be placed to divide the fish with equal areas on each side of the spine. A third, simple case can be considered where the fish maintains the same length, width and depth during bending despite the two sides going into tension and compression. In this case, the spine can be placed to divide the outline with an equal distance on its left and right.

Fish spines have been estimated as equidistant between the two sides by Videler and Hess (1984) and Rome and Sosnicki (1991) for carp and by Jayne and Lauder (1995a) for the largemouth bass. Rome and Sosnicki (1991) justified their approach by stating that differences in position between the

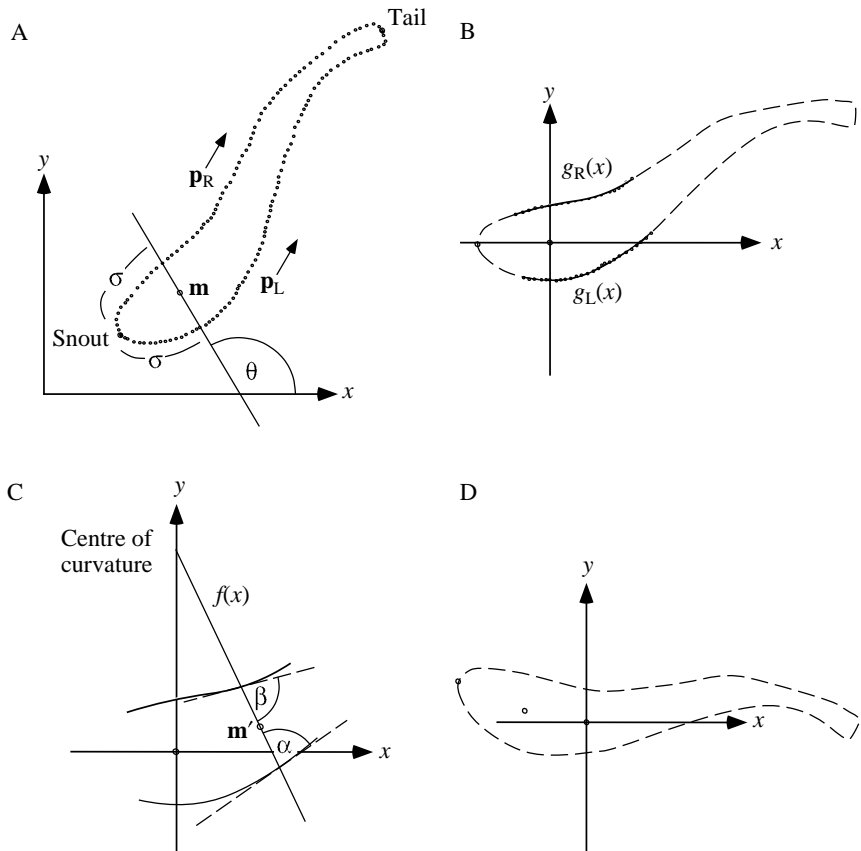


Fig. 13. The procedure for finding successive points along the spine. (A) Points around the fish outline are digitized and given position vectors  $\mathbf{p}_R$  and  $\mathbf{p}_L$  for the right and left sides, respectively. The first chord intersects the sides at an equal distance  $\sigma$  around the perimeter from the snout. Position vector  $\mathbf{m}$  describes the midpoint of this chord, and the chord intersects the  $x$ -axis with angle  $\theta$ . (B) The outline is translated to put the midpoint on the origin with the chord parallel to the  $y$ -axis. Segments of the outlines near the origin are described by the cubic functions  $g_R(x)$  and  $g_L(x)$ . (C) A new chord  $f(x)$  is constructed which intersects the two sides of the outline with equal angles  $\alpha$  and  $\beta$ . A new midpoint  $\mathbf{m}'$  is placed on the chord, and the chord intersects the  $y$  axis at the centre of curvature for that segment. (D) The outline is again translated to put the new midpoint on the origin with the new chord parallel to the  $y$ -axis. The spine-fitting procedure is repeated.

estimated spine and that visualised by X-ray photography were negligible. Carp spines have also been estimated as dividing the areas of the two sides equally by van Leeuwen *et al.* (1990); this method was similarly justified by X-ray evidence. Johnston *et al.* (1995), following the procedures and assumptions of van Leeuwen *et al.* (1990), similarly estimated spines in the short-horn sculpin *M. scorpius* to divide the areas equally. The methods given here will locate the spine according to these three hypotheses and will additionally place it in any intermediate position. The validity of the three methods was assessed using X-ray photographs of *M. scorpius* and is discussed at the end of this section.

The fish outline was separated into a number of segments, with the spine being positioned within each of these. For a straight fish, these segments form transverse sections through its body and the transverse boundaries are all perpendicular to the longitudinal body axis and parallel to each other. When the fish bends, the boundaries to the segments must remain perpendicular to the section of spine through which they intersect. However, these boundaries will no longer be parallel, as is the case for usual transverse sections. An approximation to the spine length within each segment was given by the arc length  $\sigma$  ( $=L/10$ ). This resulted in the spine being fitted to approximately 10 sections within each outline.

The fish outline was initially digitized on orthogonal  $x, y$ -axes with two series of coordinates running from snout to tail. Each series consisted of approximately 80 points (termed  $i$  and  $j$ ) and ran from the snout to the tail along either the left or right side of the body. The position vectors for these points were given by  $\mathbf{p}_{L,i}$  and  $\mathbf{p}_{R,j}$  for the left and right sides, respectively.

In order to estimate the initial orientation of the head, it was assumed that the image of the head is bilaterally symmetrical about the axis joining the snout to the base of the cranium. This is a reasonable assumption as the head outline is determined largely by the cranium, which is a symmetrical and rigid structure.

A matched pair of points on the left and right side was formed by points that are the same distance from the snout around the perimeter of the head (Fig. 13A). The first points on each side to match or exceed the distance  $\sigma$  from the snout were taken as such a pair:

$$\sum_{i=1}^p |\mathbf{p}_{L,i+1} - \mathbf{p}_{L,i}| \leq \sigma < \sum_{i=1}^{p+1} |\mathbf{p}_{L,i+1} - \mathbf{p}_{L,i}|, \quad (\text{A18})$$

and

$$\sum_{j=1}^q |\mathbf{p}_{R,j+1} - \mathbf{p}_{R,j}| \leq \sigma < \sum_{j=1}^{q+1} |\mathbf{p}_{R,j+1} - \mathbf{p}_{R,j}|, \quad (\text{A19})$$

where  $p$  and  $q$  are chosen to satisfy the inequality and identify the position of the points within each respective data series.

The line joining the points  $\mathbf{p}_{L,p}$  and  $\mathbf{p}_{R,q}$  is a chord across the fish and has a direction  $\theta$  relative to the  $x$ -axis. This chord is

perpendicular to the direction the head faces. The angle  $\theta$  is calculated using a scalar product of the vectors:

$$\theta = \arccos \left\{ \frac{(\mathbf{p}_{R,q} - \mathbf{p}_{L,p}) \cdot \begin{pmatrix} 1 \\ 0 \end{pmatrix}}{|\mathbf{p}_{R,q} - \mathbf{p}_{L,p}|} \right\}. \quad (\text{A20})$$

The midpoint of the head that lies between  $\mathbf{p}_{L,p}$  and  $\mathbf{p}_{R,q}$  is given by the position vector  $\mathbf{m}$ :

$$\mathbf{m} = \frac{\mathbf{p}_{L,p} + \mathbf{p}_{R,q}}{2}. \quad (\text{A21})$$

This position  $\mathbf{m}$  forms the first of the predicted coordinates for the spine.

Each time the spine was predicted for a segment of fish, the outline of the whole fish was translated so that the midpoint  $\mathbf{m}$  lay on the origin and rotated so that the latest chord lay along the  $y$ -axis (Fig. 13B,D). This transformation is described by:

$$\mathbf{p}' = \begin{pmatrix} \sin \theta & -\cos \theta \\ \cos \theta & \sin \theta \end{pmatrix} (\mathbf{p} - \mathbf{m}), \quad (\text{A22})$$

where  $\mathbf{p}$  is the fish coordinates in its previous orientation ( $\mathbf{p}_{L,p}$ ,  $\mathbf{p}_{R,q}$ , and the coordinates of the spine) and  $\mathbf{p}'$  is the set of transformed coordinates.

Least-squares cubic regressions were fitted to the position data for the left and for the right sides. These lines were fitted to a subset of the data which spanned the region where the new spine segment would fit, i.e. where  $-0.5\sigma \leq x < 2\sigma$ . The regressions are described by the functions  $g_L(x)$  and  $g_R(x)$  which describe the local shape of the left and right outlines respectively (Fig. 13B).

The next chord was taken as intersecting the left side at  $x=\sigma$ . The coordinates for this point are  $[\sigma, g_L(\sigma)]$ , and the tangent to the left side has a gradient  $\dot{g}_L(\sigma)$  at this point, where a dot above the variable indicates differentiation with respect to  $x$ .

The chord was initially considered to be perpendicular to the tangent at  $[\sigma, g_L(\sigma)]$ , i.e. its initial gradient was  $-1/\dot{g}_L(\sigma)$ . The function for this initial chord estimate was given by:

$$f(x) = g_L(\sigma) + \phi(x - \sigma). \quad (\text{A23})$$

The chord  $f(x)$  intersects the right side outline where  $f(x) = g_R(x)$ . This equation can be solved using Newton-Raphson iteration:

$$x_{i+1} = x_i - \frac{f(x_i) - g_R(x_i)}{f'(x_i) - \dot{g}_R(x_i)} \quad (\text{A24})$$

with the  $x$  coordinate for the intersection being termed  $\tilde{\sigma}$ . The gradient of the tangent to the right side where it intersects the chord is  $\dot{g}_R(\tilde{\sigma})$ .

The chord  $f(x)$  thus intersected the left and right sides with angles  $\alpha$  and  $\beta$  respectively, where:

$$\alpha = \arctan(\phi) - \arctan[\dot{g}_L(\sigma)] \quad (\text{A25})$$

and

$$\beta = \pi - \arctan(\phi) + \arctan[\dot{g}_R(\tilde{\sigma})]. \quad (\text{A26})$$

The chord  $f(x)$  is fitted correctly when it intersects the left and right sides with equal angles, i.e. where  $\alpha - \beta = 0$  (Fig. 13C). If  $\alpha > \beta$ , then the chord must be swung clockwise; conversely, if  $\alpha < \beta$ , then the chord must be swung anticlockwise. The appropriate adjustment to  $\phi$  was made, remembering that to swing the chord through the  $y$ -axis the gradient will approach infinity (or  $-\infty$ ) and must then change sign and decrease (or increase) in value. The process was iterated from equation A24 until  $|\alpha - \beta| < \pi/500$ .

The intersection between  $f(x)$  and the  $y$ -axis may be considered to be the centre of curvature for this segment of the spine. As discussed previously, the spine may act to divide the distance, the area or the volume of the fish equally between its two sides. If the position vector for the centre of curvature is  $\mathbf{p}_C$ , the intercept of the chord with the left side is  $\mathbf{p}_L$  and of the chord with the right side is  $\mathbf{p}_R$ , then the position of the spine  $\mathbf{m}$  on the chord is given by:

$$\mathbf{m} = \mathbf{p}_C + \left( \frac{(\mathbf{p}_L - \mathbf{p}_C)^\kappa + (\mathbf{p}_R - \mathbf{p}_C)^\kappa}{2} \right)^{1/\kappa}, \quad (\text{A27})$$

where  $\kappa$  takes the values 1, 2 or 3 for dividing the fish by width, area or volume, respectively. The mean radius of curvature  $\bar{r}$  for this segment is:

$$\bar{r} = |\mathbf{m} - \mathbf{p}_C|. \quad (\text{A28})$$

$\bar{r}$  is given positive values when the left side is on the outside of the curve, and negative values when it is on the inside.

The new chord intersects the  $x$  axis with an angle  $\theta$  ( $=\arctan\phi$ ), and the new coordinate for the spine position is given by  $\mathbf{m}'$ . These two values are used to transform the fish outline ready for calculations on the next segment (Fig. 13D). Hence, the procedure is repeated from equation A22.

The spine-fitting procedure is asymmetrical; the ideal arc length  $\sigma$  is used as a measure of the distance between chords only on the left side of the body and thus may not be the actual arc length along the midline. The actual arc length will be greater than  $\sigma$  if the left side of the body is on the inside of a bend and less than  $\sigma$  if it is on the outside. In order to generate a set of more evenly spaced spine markers, a varying value for  $\sigma$  was taken. A modified arc length  $\sigma'$  was thus taken for each segment where:

$$\sigma' = \frac{\sigma^2}{\delta}, \quad (\text{A29})$$

with  $\sigma$  being the intended arc length and  $\delta$  the actual arc length for the previous segment.

The spine-fitting procedure was repeated until the maximum of the remaining  $x$  values from a newly transformed section was less than  $2\sigma$ . Such a case indicated the close presence of the end of the tail. The coordinates of the tail were taken as the final coordinates for the spine position. The coordinates for the

spine positions and the outlines were then finally transformed to place the fish back in its initial position. This involved a translation and rotation, similar to that in equation A22, that mapped the vector from the snout to tail onto its original coordinates.

#### Smoothing spine data and centre of mass estimates

The spine-fitting algorithm is computationally quite lengthy, and so it is sensible to section the fish into only a few (10) segments. Where species are analysed with more vertebrae than those from the present study, then more segments should be taken during the computation. The estimated radii of curvature for the segments will thus give discrete values for the various locations along the fish. The coordinate data for the snout, predicted spine positions and tail can be used to generate a continuous estimate of spine curvature along the fish.

A cubic spline  $\mathbf{s}(i)$  was fitted to the spine positions. For any value of  $i$ ,  $\mathbf{s}(i)$  represents the position vector of a point on the spine. For  $n$  segments along the fish, there are  $n+1$  spine positions, and  $i$  takes the range 1 to  $n+1$ . For non-integer values of  $i$ , the position  $\mathbf{s}(i)$  is an interpolated position between two predicted spine positions.

The distance  $l$  along the spine from the snout for any location  $i$  is:

$$l(i) = \sum_{i=1.01}^{n+1} |\mathbf{s}(i) - \mathbf{s}(i-0.01)|, \quad (\text{A30})$$

where  $i$  is incremented in steps of 0.01. The total spine length is  $l(n+1)$ , and so the non-dimensional distance  $\hat{l}$  along the spine is given by:

$$\hat{l}(i) = \frac{l(i)}{l(n+1)}. \quad (\text{A31})$$

The centre of mass occurs at  $\hat{l}_1(m)$  spine lengths from the snout. Its position  $d$  along the spine was determined by solving the equation:

$$\hat{l}(d) = \hat{l}_1(m). \quad (\text{A32})$$

The coordinates for the centre of mass were thus given by the position vector  $\mathbf{s}(d)$ . The orientation  $\psi$  of the spine at this point was calculated using a scalar product of the vectors:

$$\psi = \arccos \left\{ \frac{[\mathbf{s}(d+0.01) - \mathbf{s}(d-0.01)] \cdot \begin{pmatrix} 1 \\ 0 \end{pmatrix}}{|\mathbf{s}(d+0.01) - \mathbf{s}(d-0.01)|} \right\}. \quad (\text{A33})$$

The angle between incremental sections of spine is  $\phi$  (Fig. 14). For a segment length of  $dl$ , the radius of curvature  $r(i)$  between the two segments is given by:

$$r(i) = \frac{dl}{2} \arctan \left( \frac{\pi - \phi}{2} \right). \quad (\text{A34})$$

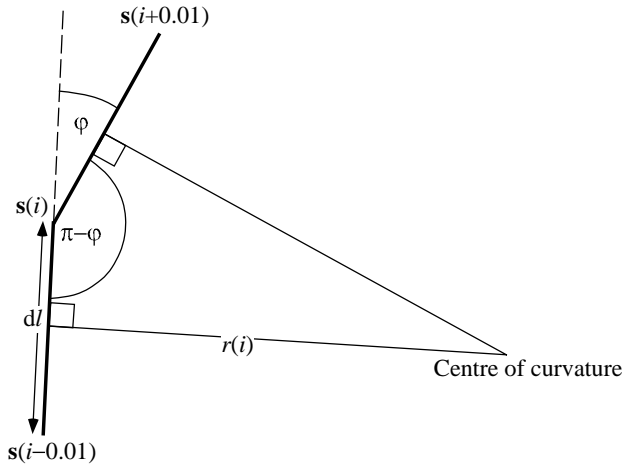


Fig. 14. The radius of curvature  $r(i)$  is calculated between successive segments along the spine. Segment length,  $d/l$ ; position vector for point on spine,  $s(i)$ ; angle between incremental segments of spine,  $\phi$ .



Fig. 15. Outlines of *Myoxocephalus scorpius* from X-ray photographs. The circles mark positions on the spine as visualized on the photographs. The coloured lines are those predicted for the spine using the methods from this study. The red line was estimated with  $\kappa=1$ , the blue using  $\kappa=2$ , and the green using  $\kappa=3$  in equation A27.

The radius of curvature asymptotes at  $\infty$  and  $-\infty$  for cases where the spine is straight. A ‘curvature’ function, being the reciprocal of radius of curvature, is more useful; a curvature of zero represents a straight section with no bending, whilst large positive and negative values for curvature represent considerable bending to the right and left, respectively. The two functions describing distance and radius of curvature along the spine  $l(i)$  and  $r(i)$ , respectively, are finally combined to

Table 5. Mean length-specific distance between the observed and predicted spines for the various values of  $\kappa$  in equation A27 (see also Fig. 15)

$\kappa$	Frame 1	Frame 2	Frame 3	Frame 4	Mean
1	0.00836	0.00752	0.00833	0.00855	0.00819
2	0.00943	0.00848	0.00796	0.01144	0.00933
3	0.01329	0.00671	0.00981	0.01467	0.01112

\* $\kappa$  is a factor defining spine position relative to the fish outline.

produce a single function  $\hat{c}(u)$  to describe the non-dimensional curvature as a function of non-dimensional distance along the fish:

$$\hat{c}(u) = \frac{l(n+1)}{r(i)}, \quad (\text{A35})$$

where  $u=\hat{l}(i)$  and takes values from 0 to 1.

Finally, a Fourier series with three terms was fitted to the curvature function  $\hat{c}(u)$  to produce a smooth, continuous estimate for the curvature along the fish.

Despite the asymmetrical nature of the fitting procedure, we found that, when this algorithm was used both on outlines and on the mirror images of those outlines, then the predicted positions of the spines were also mirror images of each other. The method is thus robust in its fitting technique.

The spine-fitting procedure was tested on digitized outlines of X-ray photographs of *M. scorpius*. A freshly killed fish was fixed in position on a polystyrene sheet using hypodermic needles, and X-ray photographs of the fish were taken. The fish was photographed in a straight position, and curving in a C- and an S-bend to each side. Values of  $\kappa$  taking 1, 2 and 3 in equation A27 were used for the spine fitting. The results from these tests are shown in Fig. 15. The predicted spines superimpose the observed one for the straight fish. For the S-bend, the change in curvature is accentuated for the higher values of  $\kappa$ ; the lowest value of  $\kappa$  gives the smoothest (least bendy) spine to fit along the fish. The mean distances between the observed and predicted spines are taken as a measure of the goodness of fit and are given in Table 5. The smallest deviation between the observed and predicted spines is shown for  $\kappa=1$ , i.e. with the spine lying equidistant between the two sides. This value of  $\kappa$  is used throughout the present study.

#### List of symbols

$a$	angular acceleration ( $\text{rad s}^{-2}$ )
$A$	acceleration ( $\text{m s}^{-2}$ )
$A_{\max}$	maximum acceleration ( $\text{m s}^{-2}$ )
$\hat{A}$	length-specific acceleration ( $=A/L$ )
$\hat{A}_{\max}$	maximum length-specific acceleration ( $=A_{\max}/L$ )
$\hat{A}_{\max, \tan}$	maximum length-specific tangential acceleration
$b$	half the width of the fish (m)
$b'$	half the depth of the fish (m)
$\hat{b}$	length-specific half-width of fish ( $=b/L$ )

$\hat{c}$	non-dimensional curvature of spine ( $=L/\text{radius of curvature}$ )	$S_k$	$k$ th moment of area
$\hat{c}()$	non-dimensional curvature of spine as a function of spine position	$\hat{S}$	non-dimensional area ( $=S/L^2$ )
$d$	interpolated segment number locating centre of mass for cubic spline	$t$	time (s)
$f()$	transverse chord through fish	$u$	non-dimensional position along spine for curvature function
$g$	gravitational acceleration constant ( $=9.81 \text{ m s}^{-2}$ )	$\hat{U}$	length-specific velocity of curvature wave along body
$g()$	section of fish outline	$v_i$	volume of $i$ th segment of fish ( $\text{m}^3$ )
$h()$	smoothing function	$V$	velocity ( $\text{m s}^{-1}$ )
$i$	segment or position number	$V_{\max}$	maximum velocity ( $\text{m s}^{-1}$ )
$I$	moment of inertia ( $\text{kg m}^2$ )	$\hat{V}$	length-specific velocity ( $=V/L$ )
$j$	frame or position number	$\hat{V}_{\max}$	maximum length-specific velocity ( $V_{\max}/L$ )
$l$	longitudinal distance from snout (m)	$V_0$	maximum fibre-length-specific contraction velocity of muscle ( $\text{s}^{-1}$ )
$\hat{l}$	non-dimensional length ( $=l/L$ )	$\alpha$	angle between tangent to fish outline and transverse chord
$\hat{l}(I)$	non-dimensional radius of the moment of inertia from the centre of mass	$\beta$	angle between tangent to fish outline and transverse chord
$\hat{l}_k(m)$	non-dimensional radius of the $k$ th moment of mass	$\delta$	spine arc length for previous segment in spine fitting
$\hat{l}_k(M)$	non-dimensional radius of the $k$ th moment of volume	$\varepsilon$	muscle strain
$\hat{l}_k(S)$	non-dimensional radius of the $k$ th moment of area	$\bar{\varepsilon}$	mean muscle strain
$l()$	distance along spine as a function of the number of predicted spine coordinates	$\phi$	gradient of chord intersecting fish outline
$\hat{l}()$	$=l()/L$	$\varphi$	angle between incremental segments of spine
$L$	maximum fish length, snout to end of tail (m)	$\eta$	hydrodynamic efficiency
$m$	body mass (kg)	$\kappa$	factor defining spine position ( $=1, 2$ or $3$ )
$m_a$	added mass (kg)	$\lambda$	gearing ratio of red to white muscle strain
$m_i$	mass of $i$ th segment of body (kg)	$\theta$	angle between $x$ -axis and transverse chord
$m_k$	$k$ th moment of mass	$\sigma$	arc length for spine fitting
$\hat{m}_m$	non-dimensional muscle mass	$\sigma'$	modified arc length for spine fitting
$\mathbf{m}$	position vector describing mid-point of transverse chord through fish	$\tilde{\sigma}$	$x$ coordinate for intersection of fish right side and transverse chord
$\mathbf{m}'$	position vector for next calculated mid-point	$\omega$	angular velocity ( $\text{rad s}^{-1}$ )
$M$	volume of fish ( $\text{m}^3$ )	$\psi$	orientation of spine at centre of mass
$M_k$	$k$ th moment of volume	<i>Further subscripts</i>	
$\hat{M}$	non-dimensional volume of fish ( $M/L^3$ )	C	centre of curvature
$n$	number (see text for details)	l	longitudinal area (from side)
$N$	number (see text for details)	L	left side of fish outline
$p$	number of point along fish outline	p	planform area (from top)
$\mathbf{p}$	position vector for point on outline of fish	red	red muscle
$\mathbf{p}'$	transformed position vector for point on outline of fish	R	right side of fish outline
$P$	power (W)	w	white muscle
$P_{\text{iner}}$	inertial power (W)	wet	wetted area (skin surface)
$P_{\text{iner,rot}}$	inertial power required for rotation (W)		
$P_t$	total hydrodynamic power (W)		
$P_{\text{use}}$	useful hydrodynamic power (W)		
$q$	number of point along fish outline		
$\mathbf{q}$	position vector for centre of mass		
$r$	radius of centre of rotation from centre of mass (m)		
$\bar{r}$	mean radius of curvature for spine segment (m)		
$r()$	radius of curvature of spine		
$s_i$	area of $i$ th segment of fish ( $\text{m}^2$ )		
$\mathbf{s}(i)$	cubic spline for position vector for the centre of the $i$ th segment		
$S$	area ( $\text{m}^2$ )		

#### Further subscripts

We would like to thank Craig Franklin and Genevieve Temple for the loan of some high speed ciné film of *N. coriiceps* and *M. scorpius*, respectively. We also thank the British Antarctic Survey for supplying live Antarctic fish and Bruno Tota for supplying the Mediterranean species. This project was funded by a grant from the Natural Environment Research Council (GR3/8814).

#### References

ALEXANDER, R. MCN. (1969). The orientation of muscle fibres in the myomeres of fishes. *J. mar. Biol. Ass. U.K.* **49**, 263–289.

- ALTRINGHAM, J. D. AND JOHNSTON, I. A. (1990). Modelling muscle power output in a swimming fish. *J. exp. Biol.* **148**, 395–402.
- ALTRINGHAM, J. D., WARDLE, C. S. AND SMITH, C. I. (1993). Myotomal muscle function at different locations in the body of a swimming fish. *J. exp. Biol.* **182**, 191–206.
- ANDERSON, M. AND JOHNSTON, I. A. (1992). Scaling of power output in fast muscle fibres of the Atlantic cod during cyclical contractions. *J. exp. Biol.* **170**, 143–154.
- BAINBRIDGE, R. (1958). The speed of swimming of fish as related to size and to the frequency and amplitude of the tail beat. *J. exp. Biol.* **35**, 109–133.
- BEDDOW, T. A., VAN LEEUWEN, J. L. AND JOHNSTON, I. A. (1995). Swimming kinematics of fast-starts are altered by temperature acclimation in the marine fish *Myoxocephalus scorpius*. *J. exp. Biol.* **198**, 203–208.
- CURTIN, N. A. AND WOLEDGE, R. C. (1988). Power output and force–velocity relationship of live fibres from white myotomal muscle of the dogfish, *Scyliorhinus canicula*. *J. exp. Biol.* **140**, 187–197.
- DOMENICI, P. AND BLAKE, R. W. (1991). The kinematics and performance of the escape response in the angelfish (*Pterophyllum eimekei*). *J. exp. Biol.* **156**, 187–205.
- DOMENICI, P. AND BLAKE, R. W. (1997). The kinematics and performance of fish fast-start swimming. *J. exp. Biol.* **200**, 1165–1178.
- EDMAN, K. A. P. (1979). The velocity of unloaded shortening and its relation to sarcomere length and isometric force in vertebrate muscle fibres. *J. Physiol., Lond.* **291**, 143–159.
- EDMAN, K. A. P. (1980). Depression of mechanical performance by active shortening during twitch and tetanus of vertebrate muscle fibres. *Acta physiol. scand.* **109**, 15–26.
- EDMAN, K. A. P., ELZINGA, G. AND NOBLE, M. I. M. (1978a). Enhancement of mechanical performance by stretch during tetanic contractions of vertebrate skeletal muscle fibres. *J. Physiol., Lond.* **281**, 139–155.
- EDMAN, K. A. P., ELZINGA, G. AND NOBLE, M. I. M. (1978b). Residual force enhancement after stretch of contracting frog single muscle fibres. *J. gen. Physiol.* **80**, 769–784.
- EKELUND, M. C. AND EDMAN, K. A. P. (1982). Shortening induced deactivation of skinned fibres of frog and mouse striated muscle. *Acta physiol. scand.* **116**, 189–199.
- ELLINGTON, C. P. (1984). The aerodynamics of hovering insect flight. II. Morphological parameters. *Phil. Trans. R. Soc. Lond. B* **305**, 17–40.
- ELLINGTON, C. P. (1985). Power and efficiency of insect flight muscle. *J. exp. Biol.* **115**, 293–304.
- FRANKLIN, C. E. AND JOHNSTON, I. A. (1997). Muscle power output during escape responses in an Antarctic fish. *J. exp. Biol.* **200**, 703–712.
- FRITH, H. R. AND BLAKE, R. W. (1995). The mechanical power output and hydrodynamic efficiency of northern pike (*Esox lucius*) fast-starts. *J. exp. Biol.* **198**, 1863–1873.
- GARLAND, T., JR AND ADOLPH, S. C. (1994). Why not to do two-species comparative studies: limitations on inferring adaptation. *Physiol. Zool.* **67**, 797–828.
- GRAY, J. (1933). Studies in animal locomotion. I. The movement of fish with special reference to the eel. *J. exp. Biol.* **10**, 88–104.
- HARPER, D. G. AND BLAKE, R. W. (1989). A critical analysis of the use of high-speed film to determine maximum accelerations of fish. *J. exp. Biol.* **142**, 465–471.
- HARPER, D. G. AND BLAKE, R. W. (1990). Fast-start performance of rainbow trout *Salmo gairdneri* and northern pike *Esox lucius*. *J. exp. Biol.* **150**, 321–342.
- HARRISON, P., NICOL, C. J. M. AND JOHNSTON, I. A. (1987). Gross morphology, fibre composition and mechanical properties of pectoral fin muscles in the Antarctic teleost *Notothenia neglecta* Nybelin. In *Fifth Congress of European Ichthyologists, Proceedings, Stockholm, 1985* (ed. S. O. Kullander and B. Fernholm), pp. 459–465. Stockholm: Swedish Museum of Natural History.
- HARVEY, P. H. AND PAGEL, M. D. (1991). *The Comparative Method in Evolutionary Biology*. Oxford: Oxford University Press.
- HUEY, R. B. (1987). Phylogeny, history and the comparative method. In *New Directions in Ecological Physiology* (ed. M. E. Feder, A. F. Bennett, W. W. Burggren and R. B. Huey), pp. 76–98. Cambridge: Cambridge University Press.
- JAMES, R. S., ALTRINGHAM, J. D. AND GOLDSPIK, D. F. (1995). The mechanical properties of fast and slow skeletal muscles of the mouse in relation to their locomotory function. *J. exp. Biol.* **198**, 491–502.
- JAMES, R. S. AND JOHNSTON, I. A. (1998). Scaling of muscle performance during escape responses in the short-horn sculpin (*Myoxocephalus scorpius*). *J. exp. Biol.* **201**, 913–923.
- JAYNE, B. C. AND LAUDER, G. V. (1993). Red and white muscle activity and kinematics of the escape response of the bluegill sunfish during swimming. *J. comp. Physiol. A* **173**, 495–508.
- JAYNE, B. C. AND LAUDER, G. V. (1995a). Speed effects on midline kinematics during steady undulatory swimming of largemouth bass, *Micropterus salmoides*. *J. exp. Biol.* **198**, 585–602.
- JAYNE, B. C. AND LAUDER, G. V. (1995b). Are muscle fibres within fish myotomes activated synchronously? Patterns of recruitment within deep myomeric musculature during swimming in largemouth bass. *J. exp. Biol.* **198**, 805–815.
- JOHNSON, T. P. AND JOHNSTON, I. A. (1991). Temperature adaptation and the contractile properties of live muscle fibres from teleost fish. *J. comp. Physiol. B* **161**, 27–36.
- JOHNSTON, I. A. (1990). Cold adaptation in marine organisms. *Phil. Trans. R. Soc. Lond. B* **326**, 655–667.
- JOHNSTON, I. A., PATTERSON, S., WARD, P. AND GOLDSPIK, G. (1974). The histochemical demonstration of myofibrillar adenosine triphosphatase activity in fish muscle. *Can. J. Zool.* **52**, 871–877.
- JOHNSTON, I. A., VAN LEEUWEN, J. L., DAVIES, M. L. AND BEDDOW, T. (1995). How fish power predation fast-starts. *J. exp. Biol.* **198**, 1851–1861.
- JOSEPHSON, R. K. (1985). The mechanical power output of a tettingoid wing muscle during singing and flight. *J. exp. Biol.* **117**, 357–368.
- JOSEPHSON, R. K. (1993). Contraction dynamics and power output of skeletal muscle. *A. Rev. Physiol.* **55**, 527–546.
- KASAPI, M. A., DOMENICI, P., BLAKE, R. W. AND HARPER, D. (1992). The kinematics and performance of escape responses of the knifefish *Xenomystus nigri*. *Can. J. Zool.* **71**, 189–195.
- LANGFIELD, K. S., ALTRINGHAM, J. D. AND JOHNSTON, I. A. (1989). Temperature and the force–velocity relationship of live muscle fibres from the teleost *Myoxocephalus scorpius*. *J. exp. Biol.* **144**, 437–448.
- MACHIN, K. E. AND PRINGLE, J. W. S. (1959). The physiology of insect fibrillar muscle. II. Mechanical properties of a beetle flight muscle. *Proc. R. Soc. Lond. B* **151**, 204–225.
- MENDEZ, J. AND KEYS, A. (1960). Density and composition of mammalian muscle. *Metabolism* **9**, 184–188.
- MOON, T. W., ALTRINGHAM, J. D. AND JOHNSTON, I. A. (1991).

- Energetics and power output of isolated fish fast muscle fibres performing oscillatory work. *J. exp. Biol.* **158**, 261–273.
- RAYNER, J. M. V. (1985). Linear relations in biomechanics: the statistics of scaling functions. *J. Zool., Lond. A* **206**, 415–439.
- ROME, L. C., FUNKE, R. P., ALEXANDER, R. McN., LUTZ, G., ALDRIDGE, H., SCOTT, F. AND FREADMAN, M. (1988). Why animals have different muscle fibre types. *Nature* **335**, 824–827.
- ROME, L. C. AND SOSNICKI, A. A. (1991). Myofilament overlap in swimming carp. II. Sarcomere length changes during swimming. *Am. J. Physiol.* **260**, C289–C296.
- STEVENSON, R. D. AND JOSEPHSON, R. K. (1990). Effects of operating frequency and temperature on mechanical power output from moth flight muscle. *J. exp. Biol.* **149**, 61–78.
- SWOAP, S. J., JOHNSON, T. P., JOSEPHSON, R. K. AND BENNETT, A. F. (1993). Temperature, muscle power output and limitations on burst locomotor performance of the lizard *Dipsosaurus dorsalis*. *J. exp. Biol.* **174**, 185–197.
- TEMPLE, G. AND JOHNSTON, I. A. (1998). Testing hypotheses concerning the phenotypic plasticity of escape performance in fish of the family Cottidae. *J. exp. Biol.* **201**, 317–331.
- VAN LEEUWEN, J. L. (1992). Muscle function in locomotion. In *Mechanics of Animal Locomotion* (ed. R. McN. Alexander), pp. 191–250. Berlin: Springer-Verlag.
- VAN LEEUWEN, J. L., LANKHEET, M. J. M., AKSTER, H. A. AND OSSE, J. W. M. (1990). Function of red axial muscles of carp (*Cyprinus carpio* L.): recruitment and normalized power output during swimming in different modes. *J. Zool., Lond.* **220**, 123–145.
- VIDELER, J. J. (1993). *Fish Swimming*. London: Chapman & Hall.
- VIDELER, J. J. AND HESS, F. (1984). Fast continuous swimming of two pelagic predators, saithe (*Pollachius virens*) and mackerel (*Scomber scombrus*): a kinematic analysis. *J. exp. Biol.* **109**, 209–228.
- WEBB, P. W. (1978). Fast-start performance and body form in seven species of teleost fish. *J. exp. Biol.* **74**, 211–226.
- WEBB, P. W. (1982). Fast-start resistance of trout. *J. exp. Biol.* **96**, 93–106.
- WEIHS, D. (1973). The mechanism of rapid starting of a slender fish. *Biorheology* **10**, 343–350.
- WEIS-FOGH, T. AND ALEXANDER, R. McN. (1977). The sustained power output from striated muscle. In *Scale Effects in Animal Locomotion* (ed. T. J. Pedley), pp. 511–525. London: Academic Press.